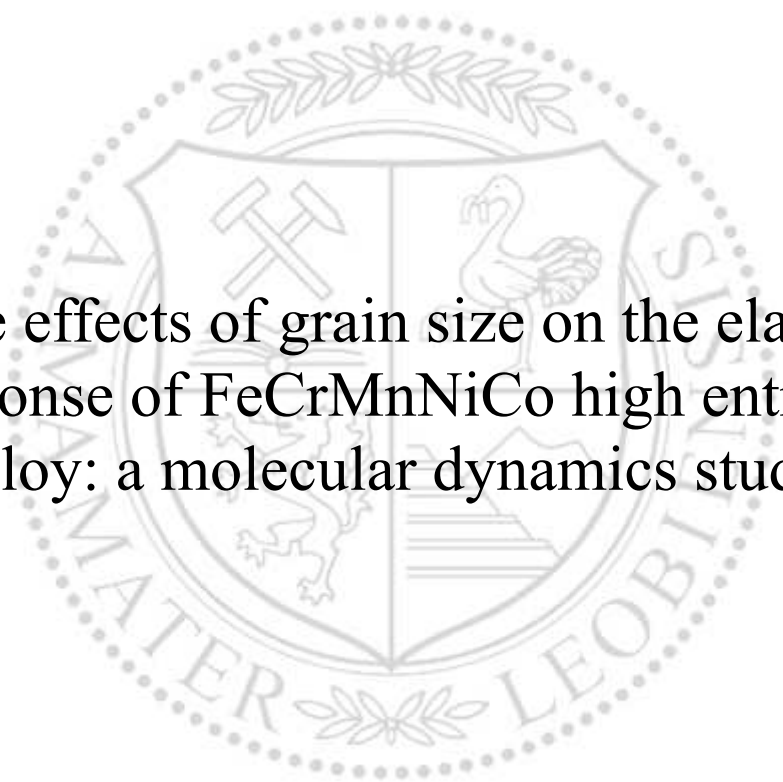




Chair of Physical Metallurgy

Master's Thesis



The effects of grain size on the elastic response of FeCrMnNiCo high entropy alloy: a molecular dynamics study

Keegan Zetterberg

August 2023



AFFIDAVIT

I declare on oath that I wrote this thesis independently, did not use other than the specified sources and aids, and did not otherwise use any unauthorized aids.

I declare that I have read, understood, and complied with the guidelines of the senate of the Montanuniversität Leoben for "Good Scientific Practice".

Furthermore, I declare that the electronic and printed version of the submitted thesis are identical, both, formally and with regard to content.

Date 31.08.2023

A handwritten signature in black ink, appearing to read 'Keegan Zetterberg'.

Signature Author
Keegan Zetterberg

Acknowledgements

Throughout my time at Universität des Saarlandes and Montanuniversität Leoben, I had many opportunities for growth in both my professional and personal life. Being part of an Erasmus+ program enabled me to study and work with incredible students from all over the world, which is an incredible opportunity in and of itself. I would like to thank all of my friends, peers, and professors, especially the following.

First and foremost, I would like to thank Christian Stehr at Oregon State University and Universität des Saarlandes for sharing the AMASE (Advanced Materials Science and Engineering) program with me. Without you, I wouldn't be here and have had these incredible experiences.

To David Holec and Thomas Leiner at Montanuniversität Leoben, who graciously took me in as a master's student, and gave me countless opportunities to meet with and present to professors relating to my work. I was able to learn a lot from both of you, which I am very grateful for.

Next, I would like to thank Martin Müser at Universität des Saarlandes for igniting my passion for computational material physics.

And most importantly, the rest of my friends and family who have supported me from the very beginning.

Contents

Contents	7
Abstract	1
Kurzfassung	3
1 Introduction	5
2 Computational Methods	7
2.1 Molecular Dynamics	7
2.2 Potentials	8
2.2.1 Lennard-Jones	9
2.2.2 Embedded Atom Method and Modified Embedded Atom Method . .	10
2.3 Thermostats and Ensembles	11
2.4 Calculation Setups	12
2.4.1 Coefficient of Thermal Expansion	12
2.4.2 Elastic Constants	13
2.4.3 Hardness	15
3 Microstructure Generation and Equilibration	17
3.1 Motivation	17
3.2 Simulation	18
3.3 Results	19

3.4 Discussion	20
4 Coefficient of Thermal Expansion Calculation	23
4.1 Motivation	23
4.2 Simulation	23
4.3 Results	23
4.4 Discussion	24
5 Influence of Temperature on Elastic Constants	25
5.1 Motivation	25
5.2 Simulation	26
5.3 Results	27
5.4 Discussion	32
6 Influence of Grain Size on Elastic Constants	33
6.1 Motivation	33
6.2 Simulation	33
6.3 Results	34
6.4 Discussion	35
7 Nanoindentation	39
7.1 Motivation	39
7.2 Simulation	40
7.3 Results	46
7.4 Discussion	47
8 Summary	53
9 Conclusions	55
Bibliography	57

Abstract

In this work, molecular dynamics was used to investigate the effect of grain size and temperature on the elastic constants and hardness of CoCrFeMnNi high entropy alloy through atomistic simulations. Grain sizes of up to 4 nm to 20 nm were simulated, across a temperature range of 100 to 1000 Kelvin.

The systems were equilibrated using a conjugate gradient style minimization followed by an NpT ensemble. Elastic constants were calculated using the deformation method, and for polycrystalline systems, averaged using Hill's averaging method. When available, the results proved to be well in agreement with experiment and other atomistic simulations. The elastic constants were found to increase with grain size on this scale.

In addition to the elastic response, the plastic response was quantified by calculating the hardness through nanoindentation. The grain size effects on flow stress were examined, and this work shows an inverse Hall-Petch relationship for the Cantor alloy.

Kurzfassung

In dieser Arbeit wurde durch Molekulardynamik die Auswirkung von Korngröße und Temperatur auf die elastischen Konstanten und die Härte der hochentropischen Legierung CoCrFeMnNi durch atomistische Simulationen untersucht. Es wurden Korngrößen von bis zu 4 nm bis 20 nm in einem Temperaturbereich von 100 bis 1000 Kelvin simuliert.

Die Systeme wurden durch eine konjugierte Gradienten-Minimierung, gefolgt von einem NpT-Ensemble, ins Gleichgewicht gebracht. Die elastischen Konstanten wurden mit der Deformationsmethode berechnet und für polykristalline Systeme mit der Hill'schen Mittelungsmethode gemittelt. Soweit verfügbar, stimmten die Ergebnisse gut mit Experimenten und anderen atomistischen Simulationen überein. Es wurde festgestellt, dass die elastischen Konstanten mit der Korngröße auf dieser Skala zunehmen.

Neben der elastischen Reaktion wurde auch die plastische Reaktion durch Quantifizierung der Härte mittels Nanoindentation berechnet. Die Auswirkungen der Korngröße auf die Fließspannung wurden untersucht, und diese Arbeit zeigt eine inverse Hall-Petch-Beziehung für die Cantor-Legierung.

Introduction

The discoveries of traditional alloys with one dominant element have often led to great societal and technological advancements for the human race. The early alloying of tin and copper led to the Bronze Age, and around 2000 years later steel was discovered by alloying iron and carbon. Since the Bronze Age, there has been exhaustive research conducted on and use of alloys with one dominant or prominent element. Traditional alloys have led to great advancements and outstanding materials, but there are still many areas to be explored. An alloy with many elements but without a dominant element greatly increases the degrees of freedom and therefore the possible materials, properties, and applications.

These materials, called multi-principle element alloys or high-entropy alloys (HEAs) have been studied since as early as the late eighteenth century by the German metallurgist Franz Karl Achard [1, 2]. About two centuries later, the separate works of Brian Cantor and Jien-Wei Yeh discovered and reported stable single-phase HEAs [3, 4]. Since 2004 extensive research has been conducted on these HEAs. Some have shown to have superior mechanical properties such as high ductility at low temperature [5, 6], high yield strength at high temperature [7], high fracture toughness [8], and a high endurance limit [9, 10]. One of the most studied HEAs is CrMnFeCoNi alloy, or Cantor alloy, due to its excellent low temperature ductility and fracture toughness. The uses and applications of Cantor alloy may include biomedical alternatives, aerospace engines, and nuclear reactors [11].

The hardness of a material, defined as the resistance against plastic deformation, permanent indentation, scratching, etc. is an important material property for engineers to consider while designing and choosing a material. Hardness has a strong correlation with wear resistance [12, 13], which is necessary to be examined for moving parts, or parts subject to frequent or continuous fluid flow. Microhardness is typically measured by either a Knoop test, Brinell test, Vicker's test, or Rockwell test. Hardness on the nanoscale, measured through nanoindentation, is the preferred method for surface properties of thin films and many bio-materials [14–16].

Other quite critical material properties are the elastic constants. For novel materials, the Young's modulus is often one of the first material properties to be examined. The Young's modulus, along with the shear modulus and Poisson's ratio, describes how the material will deform under stresses below the material's yield strength.

This thesis mainly focuses on the elastic constants and hardness dependencies of Cantor alloy, with respect to temperature and grain size. Additionally, this paper serves to demonstrate the usability of a Lennard-Jones style potential [17] for polycrystalline applications at finite temperature.

Computational Methods

2.1 Molecular Dynamics

Since its development in the 1950s, classical molecular dynamics (MD) has been used to simulate and model atomic, polymeric, biological, metal, ceramic, macroscopic, and more systems. The main advantage of MD, compared to density functional theory (DFT), is the scale of the simulations possible. DFT calculations typically only treat hundreds of atoms, while MD simulations can model millions. While DFT is a more accurate and computationally costly method, MD is quite good at modelling larger systems or systems on larger timescales, up to μs [18]. There are 4 main steps necessary for an MD simulation, which will be described in further detail below:

1. Initial conditions: position and type of atoms, boundaries, units, etc.
2. A potential or force field to describe the interactions between particles
3. An algorithm or integrator to integrate Newton's equations of motion and update the positions and velocities of each particle, each timestep
4. An ensemble which describes and controls the thermodynamics of the system. This may include thermostatting, barostatting, energy conservation, enthalpy control, and more

There are many MD packages available, but one of the most popular for atomistic simulations for materials science is Large-scale Atomic/Molecular Massively Parallel Simulator [18], or LAMMPS. LAMMPS is a very powerful tool designed for computationally heavy calculations on parallel computers, but can also be built and used on laptops and desktop computers.

Many integrators exist for differential equations, such as the forward Euler method and Runge Kutta algorithms, but the velocity Verlet algorithm is the default integrator for

LAMMPS and the most used integrator for molecular dynamics. This is due to energy conservation. Other integrators may be faster, simpler, or more robust than the velocity Verlet algorithm, but they do not conserve energy after many timesteps and are more applicable to other systems besides MD. A simple derivation of the velocity Verlet algorithm from Taylor expansions is shown through equations (2.1), (2.2), and (2.3) [19].

Starting with the Taylor expansion of $s(t + \Delta t)$

$$s(t + \Delta t) = s(t) + \Delta t \dot{s}(t) + \frac{(\Delta t)^2}{2} \ddot{s}(t) + O((\Delta t)^3) \quad (2.1)$$

and by setting $\dot{s}(t) = v(t)$, $\ddot{s}(t) = \frac{F(t)}{m}$ and neglecting $O((\Delta t)^3)$ and higher order error terms, we simplify to

$$s(t + \Delta t) = s(t) + \Delta t v(t) + \frac{(\Delta t)^2}{2} \frac{F(t)}{m} \quad (2.2)$$

From here, we still need a way to describe $v(t)$, so by taking the derivative of Eq. (2.2), we arrive at the following

$$v(t + \Delta t) = v(t) + \frac{\Delta t}{2} \left(\frac{F(t)}{m} + \frac{F(t + \Delta t)}{m} \right) \quad (2.3)$$

At this point, with starting initial conditions s_0 and v_0 and an equation or force field to describe F as a function s and/or t , we can translate the equations into a pseudocode for the velocity Verlet algorithm, shown in algorithm (1).

Algorithm 1 Velocity Verlet

```

Define  $s_0, v_0, \Delta t$  and  $F$ 
for  $iteration = 1, 2, \dots$  do
    Compute position  $s_{i+1} = s_i + \Delta t v_i + \frac{(\Delta t)^2}{2} \frac{F_i}{m}$ 
    Compute velocity  $v_{i+1} = v_i + \Delta t \frac{F_{i+1} + F_i}{2m}$ 
end for

```

This algorithm and integrator can be applied relatively easily to 2D and 3D for many-body systems.

2.2 Potentials

In order to appropriately model a system in LAMMPS, it is extremely important to use the correct potential for the system. The potential must accurately calculate the force field acting on each particle defined. There are many styles of potentials for MD available in LAMMPS, including but not limited to, pairwise potentials, machine-learned potentials, many-body potentials, potentials designed for polymers, semi-empirical potentials, and electron force fields.

2.2.1 Lennard-Jones

Pairwise potentials such as Lennard-Jones or Mie are typically not used for FCC metals. One of the primary reasons for this is that the resulting model is often much more brittle than what is observed experimentally. This is due to the Cauchy relation $\frac{C_{12}}{C_{44}}$ of FCC metals being ca. 1.5-3, while pairwise potentials such as the Lennard-Jones or Mie potential tend towards giving a Cauchy relation of 1 [20]. The Cauchy relation is a criterion for the ductility of a material, with a value of less than 1 being a brittle material and a value larger than 1 being a ductile material. This is equivalent to the Cauchy pressure, $C_{12} - C_{44}$, where ductile FCC metals have large Cauchy pressures.

However, as described by Gröger in [17], the Cauchy pressure of the Cantor alloy is low, which leads the Cauchy relation to be close to 1 [21, 22], the same as a Lennard-Jones material. Specifically, the Cauchy pressure $C_{12} - C_{44}$ of Cantor alloy is an order of magnitude lower than any of the elastic constants C_{11} , C_{12} , and C_{44} . Additionally, due to the randomness of the equiatomic structure, we expect 75% or 80% of the nearest neighbors to be between unlike atoms, for quaternary and quinary systems respectively. With the combination of these two points, it is argued by Gröger that pair interactions are the dominant component of bonding within the alloy.

The Lennard-Jones model defines the pairwise energy contribution to a particle from its neighbors as

$$U = \sum_{i=1}^N 2\epsilon \left[\left(\frac{\sigma}{r_i} \right)^{12} - \left(\frac{\sigma}{r_i} \right)^6 \right] \quad (2.4)$$

where N is the number of neighbors, r_i is the distance between the neighbor particle i and the center particle, ϵ is the absolute minimum of the potential energy curve, and σ is the distance at which the potential energy is zero. The 12th power term of the equation describes the repulsive forces due to overlapping electron clouds, and the 6th power term describes the attractive Van der Waals forces between particles. A second summation can be added to loop over all pairs in a system, as shown below.

$$U = \frac{1}{2} \sum_{i=1}^N \sum_{j=1, j \neq i}^N 2\epsilon \left[\left(\frac{\sigma}{r_{ij}} \right)^{12} - \left(\frac{\sigma}{r_{ij}} \right)^6 \right] \quad (2.5)$$

It is important to exclude self interactions, where $i = j$, as this would lead to diverging energy. The force contributions, defined as $-\frac{dU}{dr}$, can be tabulated and then summed for efficient computing. A section of the $U(r)$ potential energy curve between two atoms is shown in Fig. 2.1.

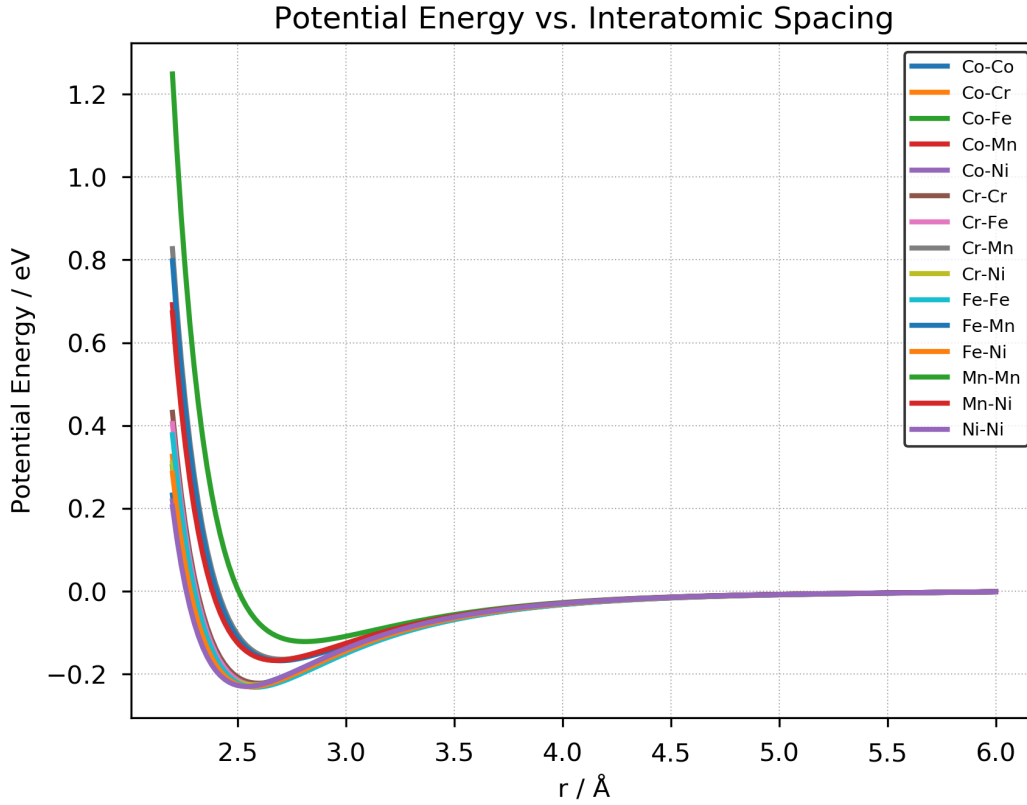


Figure 2.1: The potential energy between two atoms of interatomic distance r . The potential was generated by Gröger et al. [17].

2.2.2 Embedded Atom Method and Modified Embedded Atom Method

Many-body potentials, such as the embedded atom method (EAM) and modified embedded atom method (MEAM) are the most popular potentials to model FCC metals [20], because they balance accuracy and efficiency. Large scale simulations are still possible, though they take longer than simulations run with simpler potentials. The EAM, as proposed by Daw and Baskes [23], seeks to better model close packed metals than pairwise potentials by including more information in a more complicated potential form. The energy of an atom E_i , described by the EAM is shown in Eq. 2.6

$$E_i = F_\alpha \left[\sum_{j \neq i} \rho_\beta(r_{ij}) \right] + \frac{1}{2} \sum_{j \neq i} \phi_{\alpha\beta}(r_{ij}) \quad (2.6)$$

where ϕ is the pairwise interaction potential between atoms i and j based on electrostatics, r_{ij} is the distance between atoms i and j , $F(\rho)$ is an embedding function that depends on the local electron density ρ around the atom i , and α and β are the element types of atoms i and j , respectively.

The MEAM potential, first proposed by Baskes [24], is based on the EAM but takes into

account angular forces, allowing covalently bonded materials to be modelled in addition to metals. The EAM approximates the local electron density around each atom is a sphere in shape, while the MEAM takes bond orientation into account.

The energy of an atom E_i using the MEAM is calculated using the same formula as the EAM, shown in Eq. 2.6. However, the angular forces are included while calculating the electron density, ρ , by separating ρ into partial electron background densities. These are scaled depending on the x, y, z components of the distances between two atoms.

A MEAM potential for Cantor alloy [25] was used in the early stages of this work, but was replaced by the Lennard-Jones potential due to an increased computational efficiency of ~ 10 times, and more accurate results for calculated elastic constants. A direct comparison of the results from these two methods is shown in Chapter 3.

2.3 Thermostats and Ensembles

The next step in setting up the simulation is to describe how and which system parameters can be controlled. Widely used ensembles for molecular dynamics simulations include the microcanonical (NVE), canonical (NVT), isothermal-isobaric (NpT), and isenthalpic (NpH) ensembles, though others exist. Ensembles describe how the energy, temperature, pressure, etc. are controlled or maintained throughout the simulation [26–28].

The earliest ensemble used for MD simulations was the NVE ensemble (constant number of particles, volume, and energy), since it suitable for modelling a wide range of situations. However, it is sometimes of interest to control the temperature and/or pressure of the system, and allow the volume and/or energy of the system to fluctuate. The earliest examples of this includes phase changes in chemical reactions, where the system could heat up at an unrealistic rate, accelerating the reaction or destroying the new phase [26]. With an NpT or NpH ensemble, these issues would be avoided, as energy could be dissipated at a realistic rate, allowing the system to be modelled further. The earliest methodology for applying constant temperature or constant temperature ensembles in molecular dynamics is described by Andersen et al. [26].

In the simulations described in this paper, NpT is the most often used ensemble. NpT (constant number of particles, pressure, and temperature) thermostats the system by adding a damping factor and random velocity to each particle. A barostat also controls the system pressure, by adjusting the simulation boundary dimensions. During simulations with constant volume, NVE is used along with a Langevin thermostat. The microcanonical ensemble is the best method for conserving energy.

2.4 Calculation Setups

2.4.1 Coefficient of Thermal Expansion

The linear coefficient of thermal expansion, or CTE, of a material is necessary for engineers to know, especially while designing structural, performance, or composite parts. The CTE is used to calculate internal stresses due to temperature fluctuations. The residual stresses from manufacturing composite materials such as ceramic matrix composites and carbon fiber reinforced plastics can also be calculated using the CTE of the materials [29].

In engineering practice, it is sometimes enough to approximate the CTE of a material as a constant value. The average coefficient of thermal expansion over a set temperature range can be calculated as

$$\alpha_{\text{avg}} = \frac{L_2 - L_1}{L_1} \frac{1}{T_2 - T_1} \quad (2.7)$$

where α_{avg} is the average coefficient of thermal expansion. T_1 and T_2 are the initial and final temperatures, respectively. L_1 and L_2 are the initial and final lengths, respectively.

If much more data is available or the material will undergo a large temperature change, one can take the derivative of the first term with respect to temperature, which simplifies to

$$\alpha = \frac{d}{dT} \frac{L(T) - L_0}{L_0} \quad (2.8)$$

where the length L is a function of temperature T and L_0 is the initial reference length.

As shown by Van Bohmen et al. [30], the relative change in specimen length $\frac{L-L_0}{L_0}$ of austenitic steels can be reasonably fit to the exponential

$$\frac{L - L_0}{L_0} = \alpha_{HT} \cdot T + \alpha_{HT} \cdot \Theta_D \cdot (e^{-T/\Theta_D} - 1) \quad (2.9)$$

where α_{HT} is the linear coefficient of thermal expansion at the high temperature limit, T is the temperature, Θ_D is the Debye temperature, and L is the length of the sample. While this equation was originally derived to most accurately fit FCC steels [30], it also fits the experimental data of other metals [31] and the Cantor alloy [22] very well.

In order to reduce bias, the calculated data from this work will not be fit to this equation, but the derivative in Eq. 2.8 will be calculated numerically by the central difference method.

2.4.2 Elastic Constants

The most basic definition of Hooke's law relates an applied uniaxial stress (σ) on a material and the resulting strain in the same direction of the applied stress (ϵ) by the Young's modulus (E), as shown in Eq. 2.10.

$$E = \frac{\sigma}{\epsilon} \quad (2.10)$$

While this equation is applicable in simple cases and helpful for teaching the subject, a lot of useful information about the material behavior is lost. Applying the same relationship in 3 dimensions and using principles of continuum mechanics, we arrive at the more general Eq. 2.11

$$\boldsymbol{\sigma} = \mathbf{c}\boldsymbol{\epsilon} \quad (2.11)$$

where $\boldsymbol{\sigma}$ and $\boldsymbol{\epsilon}$ are second order tensors and \mathbf{c} , the stiffness tensor, is a fourth order tensor.

$$\boldsymbol{\sigma} = \begin{bmatrix} \sigma_{xx} & \sigma_{xy} & \sigma_{xz} \\ \sigma_{yx} & \sigma_{yy} & \sigma_{yz} \\ \sigma_{zx} & \sigma_{zy} & \sigma_{zz} \end{bmatrix} \quad (2.12)$$

$$\boldsymbol{\epsilon} = \begin{bmatrix} \epsilon_{xx} & \epsilon_{xy} & \epsilon_{xz} \\ \epsilon_{yx} & \epsilon_{yy} & \epsilon_{yz} \\ \epsilon_{zx} & \epsilon_{zy} & \epsilon_{zz} \end{bmatrix} \quad (2.13)$$

The stiffness tensor \mathbf{c} , which has 81 components, can be simplified due to the geometry and symmetry of physical materials to between 2 and 21 individual components. The resulting equation for an anisotropic material in Voigt notation also simplifies $\boldsymbol{\sigma}$ and $\boldsymbol{\epsilon}$ due to geometry and symmetry, leading to a simpler form, shown in Eq. 2.14.

$$\begin{bmatrix} \sigma_{11} \\ \sigma_{22} \\ \sigma_{33} \\ \sigma_{23} \\ \sigma_{13} \\ \sigma_{12} \end{bmatrix} = \begin{bmatrix} C_{11} & C_{12} & C_{13} & C_{14} & C_{15} & C_{16} \\ & C_{22} & C_{23} & C_{24} & C_{25} & C_{26} \\ & & C_{33} & C_{34} & C_{35} & C_{36} \\ & & & C_{44} & C_{45} & C_{46} \\ & & & & C_{55} & C_{56} \\ & & & & & C_{66} \end{bmatrix} \begin{bmatrix} \epsilon_{11} \\ \epsilon_{22} \\ \epsilon_{33} \\ 2\epsilon_{23} \\ 2\epsilon_{13} \\ 2\epsilon_{12} \end{bmatrix} \quad (2.14)$$

where the stiffness tensor is symmetric along the diagonal.

There are a few different approaches to determine the stiffness tensor using molecular dynamics. The method used in this paper, the stress-strain method, works by applying a

defined strain deformation in each of the 6 defined modes ($\epsilon_{11}, 2\epsilon_{23}, etc.$) shown in 2.14, and calculating the resulting stresses. The strain is applied in both the positive and negative directions, and by using this data, the stresses are then averaged.

Since the Cantor alloy is a cubic system, the elastic constants can be defined by 3 independent values: C_{11} , C_{12} , and C_{44} . These values will be calculated and plotted for the monocrystalline systems in Chapter 5.

For polycrystalline systems, the most applied method used for calculating average elastic constants in the literature is the Hill averaging scheme. Derived from and using aspects of Voigt [32] and Reuss [33], Hill's averaging method [34] can more accurately calculate the elastic constants: Young's modulus, shear modulus, bulk modulus, and Poisson's ratio. The equations for a cubic crystal using Voigt's method are:

$$B_v = \frac{1}{3}(C_{11} + 2C_{12}) \quad (2.15)$$

$$G_v = \frac{1}{5}(C_{11} - C_{12} + 3C_{44}) \quad (2.16)$$

with B and the bulk modulus and G as the shear modulus. These calculated by Reuss' methods are:

$$B_r = \frac{1}{3}(C_{11} + 2C_{12}) \quad (2.17)$$

$$G_r = \frac{5(C_{11} - C_{12})C_{44}}{4C_{44} + 3(C_{11} - C_{12})} \quad (2.18)$$

Hill's method averages these values, so

$$B = \frac{B_v + B_r}{2} \quad (2.19)$$

$$G = \frac{G_v + G_r}{2} \quad (2.20)$$

$$E = \frac{9GB}{3B + G} \quad (2.21)$$

$$\nu = \frac{3B - 2G}{2(3B + G)} \quad (2.22)$$

with E and ν being the Young's modulus and Poisson's ratio, respectively. This method was used to calculate the polycrystalline elastic constants in Chapter 6.

2.4.3 Hardness

While the units of hardness are pascals, the same as strength and elastic constants, the results from measuring hardness vary greatly depending on the methodology. The indenter shape, speed, and many more test parameters can greatly affect the resulting hardness value, and therefore, many hardness tests have been standardized. Those among the most popular include the Knoop test, Brinell test, Vicker's test, or Rockwell test. Each test method has a standardized indenter shape and indenter depth. A spherical indenter with indentation depths up to 5 nm were used, though the hardnesses were calculated at around 2 nm depths. In this work, the hardness H will be calculated as

$$H = \frac{F_{avg}}{A_{res}} \quad (2.23)$$

where F_{avg} is the average force acting on the indenter at the maximum indentation depth, and A_{res} is the resulting area of the imprint after the indenter is removed. It will be shown how both the force vs. displacement curves and the hardness values change with varying parameters, which will be discussed later in this thesis.

Microstructure Generation and Equilibration

3.1 Motivation

The first step of an MD simulation is to define the initial positions of the atoms. While LAMMPS does this quite easily for aligned monocrystalline monoatomic structures, it does not have the capability yet to generate an equiatomic polycrystalline microstructure of CoCrFeMnNi Cantor alloy. To do this, Nanohub [35] random structure generator was used to generate a seed file of equiatomic FCC CoCrFeMnNi. Next, AtomsK [36] was used to generate polycrystalline microstructures using the seed file from Nanohub.

Proper equilibration of an MD system simulation is often one of the most important and computationally costly steps. During the equilibration phase, the atoms are brought to a local or global minimum potential energy position, depending on the desired output of the simulation. In simple equilibrations, the temperature is maintained at 0 K and the atomic positions are algorithmically adjusted to reach a local minimum energy state, sometimes overcoming small energy boundaries to deeper potential energy wells depending on the algorithm. For equilibration at finite temperatures, it is a much more complicated procedure. The temperature, pressure, or volume of the system are typically controlled during an ensemble to regulate the phase and/or microstructure of the result. The lowest energy phase of a material modelled by a Lennard-Jones potential is hexagonal close packed (hcp) [37]. But as described by Travasset [37], an FCC phase can easily be stabilized with pressure and/or temperature.

In this chapter, the procedure and methods for equilibration at finite temperatures will be explained.

3.2 Simulation

The seed file from Nanohub and an example of the resulting microstructure are shown in Fig. 3.1.

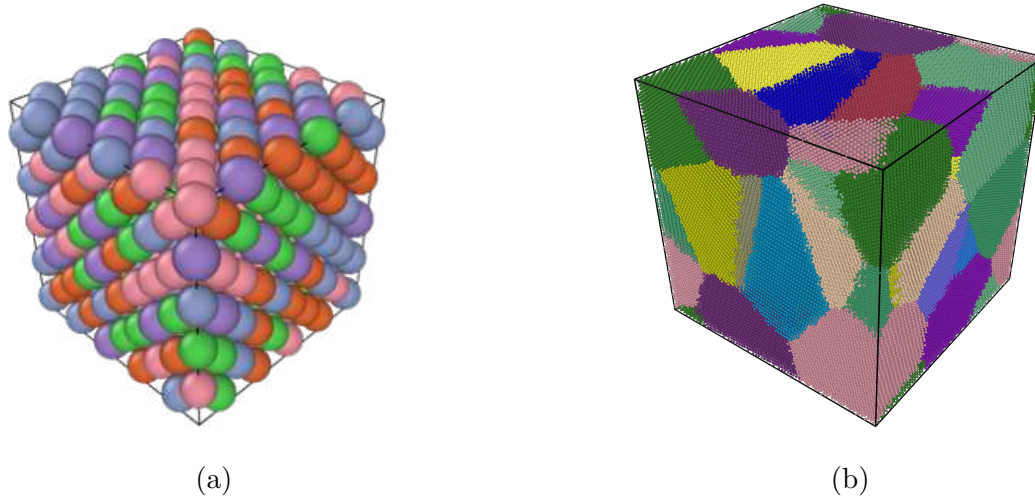


Figure 3.1: a) The seed file of equiatomic FCC CoCrFeMnNi from Nanohub [35]. b) The polycrystalline microstructure generated through Atomsk [36]. The seed and simulation cells visualized by Ovito [38].

The steps to properly equilibrate the systems at finite temperatures are as follows:

1. Delete overlapping atoms generated during defining the microstructure
2. Use a conjugate-gradient (CG) style minimization while allowing the simulation box to relax
3. Set an NpT ensemble with a target virial pressure of zero and defined target temperature
 - a) Run for a sufficient amount of time steps to allow the system to equilibrate (30-40% of time steps occur once energy has plateaued)

Since equilibrating is often one of the most costly steps of MD, care must be taken to improve efficiency. The logic behind the steps above are as follows. The positions of the atoms from Nanohub and Atomsk are perfect FCC crystals with “messy” grain boundaries. The delete overlapping atoms step serves to improve the grain boundaries, and to remove the possibility of an exploding simulation. Through testing and critical examination of Fig. 2.1, an atom within a 0.75 \AA radius of another is deleted. The calculated values of elastic constants and CTE showed almost no difference with or without this step, though equilibrating with this step was faster and never resulted in an exploding simulation.

The next step, the CG minimization while allowing the box to relax, serves two main purposes. First, it allows for local relaxations and rearrangements at the grain boundaries, and second, it brings the atoms in the bulk of grains to their positions in the distorted lattice that HEAs are known for. Since this is done while allowing the box dimensions to change anisotropically, internal stresses that may have occurred due to the grain boundaries or even an uneven distribution of lattice parameters, are relaxed. The relaxation of the simulation cell boundaries, using the ‘fix box/relax’ command in LAMMPS, allows one to define the target pressure in each of the boundary directions, and is even applicable to triclinic boxes. A basic pseudocode for a CG style minimization is shown in algorithm 2.

Algorithm 2 Conjugate Gradient (CG) minimization algorithm

```

1: procedure CG MINIMIZATION
2:   Set the initial position  $\vec{x}_0$  and force  $\vec{f}_0$ 
3:   Set the energy tolerance  $E_{break}$ 
4:   Set the force tolerance  $f_{max}$ 
5:   Set the maximum number of iterations  $n_{max}$ 
6:   Set the initial step size  $\alpha_0 = 1$ 
7:   for  $n = 0, 1, 2, \dots, n_{max} - 1$  do
8:     Calculate the energy  $E_n$  and force  $\vec{f}_n$  at the current position  $\vec{x}_n$ 
9:     Calculate the magnitude of the force  $f_n = \|\vec{f}_n\|$ 
10:    if  $f_n < f_{max}$  or  $\Delta E < E_{break}$  then
11:      break
12:    end if
13:    if  $n = 0$  then
14:      Set the search direction  $\vec{d}_n = -\vec{f}_n$ 
15:    else
16:      Calculate the beta coefficient  $\beta_n = \frac{\vec{f}_n \cdot (\vec{f}_n - \vec{f}_{n-1})}{\|\vec{f}_{n-1}\|^2}$ 
17:      Update the search direction  $\vec{d}_n = -\vec{f}_n + \beta_n \vec{d}_{n-1}$ 
18:    end if
19:    Calculate the step size  $\alpha_n = \frac{\vec{d}_n \cdot \vec{f}_n}{\|\vec{d}_n\|^2}$ 
20:    Update the position  $\vec{x}_{n+1} = \vec{x}_n + \alpha_n \vec{d}_n$ 
21:  end for
22: end procedure

```

3.3 Results

Before all the systems were to be equilibrated, the potential had to be chosen. As described in Chapter 2, there are both MEAM and Lennard-Jones potentials to model the Cantor alloy. The results comparing the equilibration results using both potentials are described in Tab. 3.1 and 3.2. The same equilibration script was tested on both a monocrystalline and polycrystalline system.

Table 3.1: MEAM vs. Lennard Jones: Monocrystalline Equilibration Results

	1 Grain MEAM	1 Grain Lennard-Jones
E_{eq} / eV	-2714246 ± 19	-1047073 ± 8
Temperature / K	300.05 ± 0.19	300.02 ± 0.23
Pressure / Bar	-0.03 ± 2.79	0.05 ± 1.76
Volume / \AA^3	8024776 ± 105	8180380 ± 124
CPU Hours	3193.2	314.4

Table 3.2: MEAM vs. Lennard Jones: Polycrystalline Equilibration Results

	7 Grains MEAM	7 Grains Lennard-Jones
E_{eq} / eV	-2717465 ± 26	-1038219 ± 10
Temperature / K	300.03 ± 0.21	300.01 ± 0.22
Pressure / Bar	0.14 ± 2.84	0.03 ± 1.61
Volume / \AA^3	8102460 ± 97	8314025 ± 138
CPU Hours	3251.5	329.7

It can be seen that the chosen potential effects the final equilibrated energy E_{eq} , final volume, and CPU hours. The temperature and pressure should not change, as those are controlled with the NpT ensemble. The volume, while changing from 8024776 \AA^3 to 8180380 \AA^3 seems like a significant change, but only signifies an increase in lattice constant of about 1%. The change in energy is likely described by the type and properties of the potential.

The results from the equilibration script are shown in Fig. 3.2.

Shown are the virial pressure, temperature, volume, and energy as a function of timestep during the NpT ensemble. While using LAMMPS, one must take care to use the correct pressure. LAMMPS defaults to the total pressure, which includes a kinetic energy term. One method to change this is to use the compute command to compute a new pressure through the virial pressure, or stress, equation, as shown in Eq. 3.1.

$$P_{ij} = \frac{1}{V} \sum_{k=1}^N \mathbf{r}_{ki} \cdot \mathbf{f}_{kj} \quad (3.1)$$

In this equation, P_{ij} is the i, j component of the LAMMPS calculated symmetric virial pressure, or stress, tensor. \mathbf{r}_{ki} and \mathbf{f}_{kj} are the i and j components of the position and force and vectors of atom k . N is the total number of particles in the system.

3.4 Discussion

As shown in Fig. 3.2b, 3.2c, and 3.2d, the temperature, volume, and energy all rise during equilibration with the NpT ensemble. This is because the previous kinetic energy of the

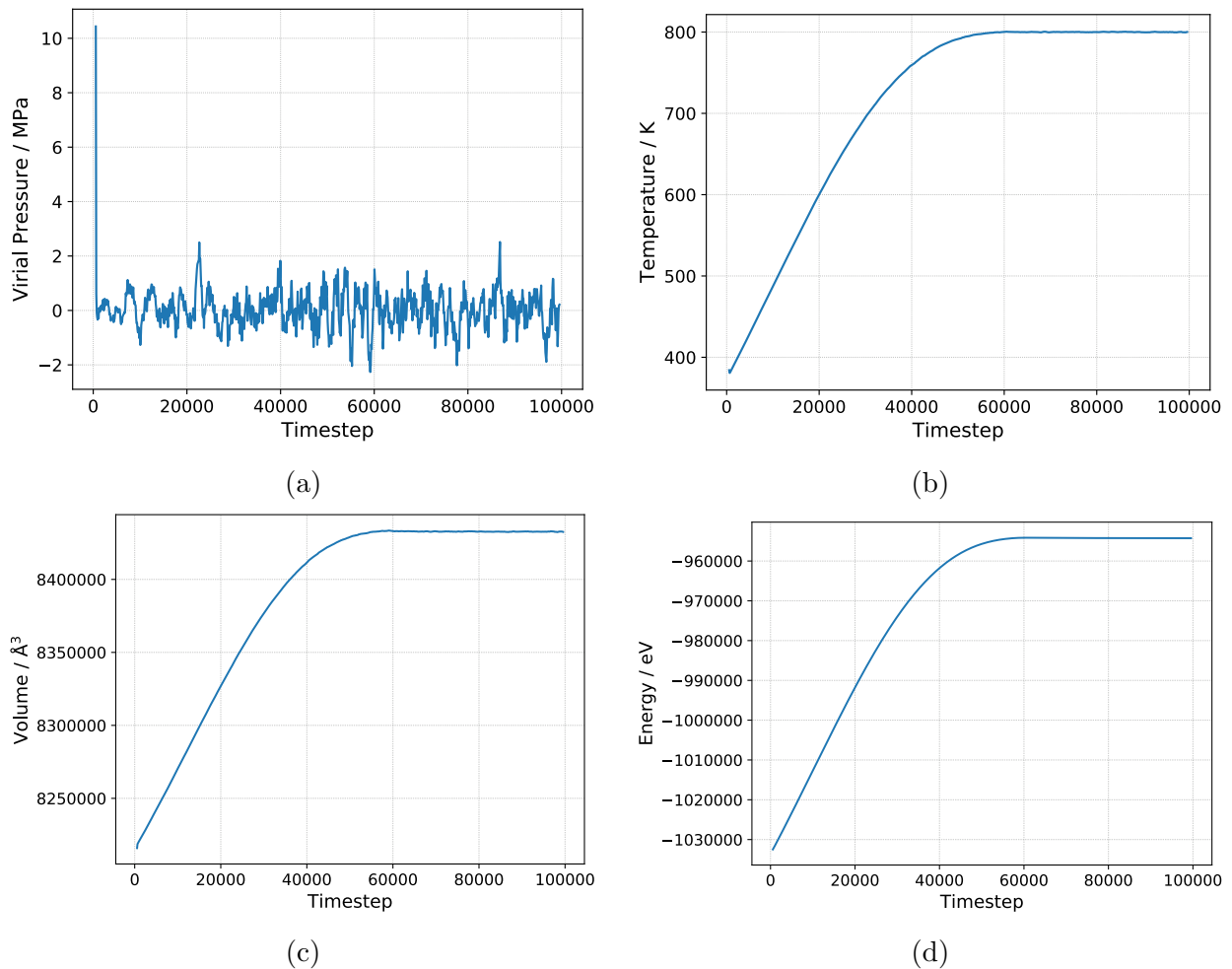


Figure 3.2: Examples of the results from the NpT ensemble of the equilibration script using the Lennard-Jones potential from Gröger et al. [17]. a) The virial pressure equilibration. b) The temperature equilibration. c) The volume equilibration. d) The energy equilibration.

system is zero after the CG minimization. The kinetic energy of the system rises with temperature, thus increasing energy. The volume of the system must increase with due to the thermal expansion of the material with an increase in temperature. The pressure on the other hand, shown in Fig. 3.2a, quickly equilibrates to zero and then fluctuates from about -2 MPa to 2 MPa.

The difference in the equilibration results using MEAM vs. Lennard-Jones, shown in 3.1 and 3.2, are quite interesting. Since the Lennard-Jones potential was shown to model the Cantor alloy by Gröger et al. [17], the resulting values should match those of MEAM [25], but they do not. This is especially true for the volume change. It was initially thought that this difference could just be at the grain boundaries, but since the final volume of the Lennard-Jones equilibrated monocrystalline system is larger than that of the MEAM equilibrated monocrystalline system, it is shown that the lattice constant is modelled to be larger using the Lennard Jones potential. The difference in calculated elastic constants will be discussed

in Chapter 5.

Coefficient of Thermal Expansion Calculation

4.1 Motivation

Calculating the coefficient of thermal expansion (CTE) is a side product of this thesis, but it provides insight on the usability of the potential for polycrystalline simulations.

4.2 Simulation

The average equilibrated volume and equilibrated temperature are calculated by averaging the last 20,000 timesteps from the results shown in figures 3.2b and 3.2c. From here, the average length is calculated as the cube-root of the simulation box volume, and $\frac{L-L_0}{L_0}$ is plotted with respect to temperature. The CTE value, α , is defined as $\frac{d}{dT} \frac{\Delta L}{L_0}$. The derivative was computed numerically through the central difference method, in order to not induce any fitting bias.

4.3 Results

Fig. 4.1a shows the relative change in specimen length $\frac{L-L_0}{L_0}$ as a function of temperature. On the right-hand side, in Eq. 4.1b, the result of the α values, calculated by the central difference method, are shown.

The simulation results from Fig. 4.1a are very similar to the experimental values from Laplanche et al. [22]. There is a slight difference in the trend of the curve, as Laplanche et al. describes an exponential fit for both FCC metals and Cantor alloy, while the data found in this work is more similar to the shape of a quadratic curve. This is more evident in Fig.

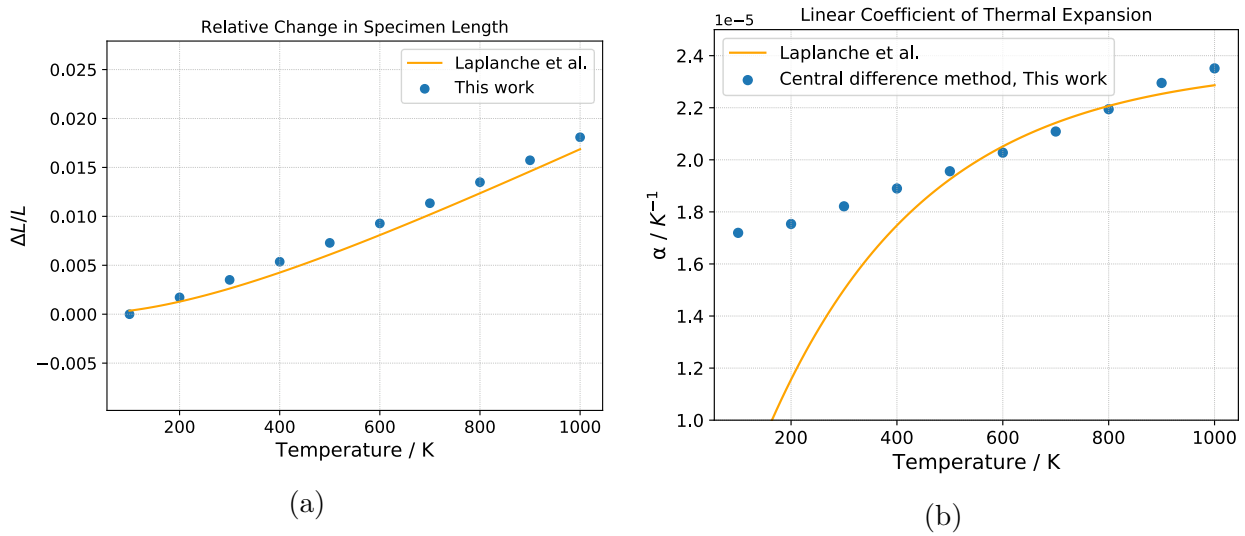


Figure 4.1: Coefficient of thermal expansion results compared to Laplanche et al. [22]. a) The plotted normalized change in length with respect to temperature. b) The calculated coefficient of thermal expansion.

4.1b, where the experimental values follow an exponential curve, but the values from this work are nearly linear. The CTE values are still quite similar for temperature values above 500 K, although there is a discrepancy between values at lower temperatures.

4.4 Discussion

The reasons for the inaccuracies at lower temperatures are unclear, though it is likely due to the simplicity of the potential. Nevertheless, this potential provides a very reasonable approximation for volume change and length change for the temperatures tested.

Since the scope of this work is mainly on the mechanical properties and the system only needed to be effectively equilibrated in this step, accurate CTE values were not necessary. If it was necessary to obtain more accurate CTE values, a potential trained on or fit to CTE data should be used.

Influence of Temperature on Elastic Constants

5.1 Motivation

Since some HEAs have been shown to have good properties, particularly at high [7] or low [5, 6] temperatures, the temperature dependency of the elastic constants for Cantor alloy should be examined. This has been done experimentally for monocrystalline systems by calculating the stiffness tensor C_{ij} [39]. Polycrystalline systems have also been investigated [21, 22, 40], calculating the polycrystalline elastic moduli: Young's modulus E , shear modulus G , bulk modulus B , and Poisson's ratio ν . There has also been DFT calculations on polycrystalline systems [41]. While the experimental results are in agreement, there is a discrepancy between the experimental results and the results from DFT. This is likely a size effect from the small simulation size of DFT, which cannot handle polycrystalline microstructures. Another possible factor for this difference is temperature. DFT corresponds to a state with no kinetic energy, or a 0K state, while experiments can only be performed at finite temperatures.

In an attempt to achieve values more similar to experiment, the elastic constants of polycrystalline Cantor alloy for a large simulation cell (20 nm x 20 nm x 20 nm) are calculated. Additionally, the stiffness tensor and independent values C_{11} , C_{12} , and C_{44} are calculated for an aligned monocrystal across various temperatures. This serves primarily to compare the results to [39] across temperatures and [17] at 0 K, to ensure that the correct methodology was being used.

In addition to the elastic constants, the Zener's anisotropy ratio is calculated. The Zener's anisotropy ratio, defined as $A = \frac{2C_{44}}{C_{11} - C_{12}}$, reflects the anisotropy of the crystal's mechanical response to deformation in different crystallographic directions. A higher anisotropy ratio depicts a greater anisotropy in the material. In metals, the Zener's anisotropy ratio has

been shown to increase with temperature [42], while the plastic anisotropy has been shown to decrease [43].

In this chapter, the calculated stiffness tensor, elastic moduli, and anisotropy ratio will be compared with experiment and DFT, across a range of temperatures.

5.2 Simulation

For both the monocrystalline and polycrystalline cases, an overview of the tests is shown below in Tab. 5.1. For the polycrystalline simulations, there were 3 unique models equilibrated and tested across the range of temperatures.

Table 5.1: Simulation Plan for Elastic Constants vs. Temperature

Temp. / K	Monocrystalline # of trials	Polycrystalline # of trials (grain size in nm)
100	1	3 (8.5)
200	1	3 (8.5)
300	1	3 (8.5)
400	1	3 (8.5)
500	1	3 (8.5)
600	1	3 (8.5)
700	1	3 (8.5)
800	1	3 (8.5)
900	1	3 (8.5)
1000	1	3 (8.5)

The temperature range of 100K to 1000K was chosen as it is a large range below the melting temperature, and is similar to the ranges of [21, 39]. While the higher temperature tests are above annealing temperatures for Cantor alloy [44], 450 °C - 1200 °C, care was taken to ensure that none of the grains disappeared due to grain growth.

Each of the 3 unique models were generated and equilibrated at each of the 10 temperatures as described in Chapter 3. The stiffness tensor was calculated as described in Chapter 2 through the LAMMPS example script. The specific and important parameters input into LAMMPS can be seen in Tab. 5.2.

Table 5.2: Parameters for Elastic Constants Calculation

Parameter / Units	Value
Timestep / ps	0.001
Thermostat damping constant / K	0.01
Applied Strain	0.02

5.3 Results

The first results to be discussed are the elastic constant results comparing using MEAM and Lennard-Jones potentials. The raw output stiffness tensor from the LAMMPS script for the monocrystalline system modelled with MEAM is:

$$C_{ij} = \begin{bmatrix} 206.7 & 149.8 & 148.1 & 0.4 & -1.1 & -0.9 \\ & 208.0 & 147.9 & 2.0 & -0.3 & -1.7 \\ & & 208.6 & 1.7 & 0.4 & -0.2 \\ & & & 73.7 & -0.3 & -0.1 \\ & & & & 74.4 & -0.4 \\ & & & & & 75.0 \end{bmatrix} \text{ GPa}$$

while the same system modelled with Lennard-Jones is:

$$C_{ij} = \begin{bmatrix} 223.3 & 128.3 & 128.9 & 0.0 & 2.7 & 1.2 \\ & 222.8 & 128.5 & -1.0 & -0.3 & 3.1 \\ & & 222.7 & -2.7 & 4.0 & -0.2 \\ & & & 123.9 & -0.5 & -0.6 \\ & & & & 124.1 & 0.3 \\ & & & & & 123.5 \end{bmatrix} \text{ GPa}$$

The averaged C_{11} , C_{12} , and C_{44} values are shown in Tab. 5.3.

Table 5.3: MEAM vs. Lennard Jones: Monocrystalline Elastic Constant Results

	1 Grain MEAM	1 Grain Lennard-Jones
C_{11} / GPa	207.8	222.9
C_{12} / GPa	148.6	128.6
C_{44} / GPa	74.3	123.8
CPU Hours	542.8	57.0

There is a significant change in the computed C_{44} values. Interestingly, the Lennard-Jones potential seems to fit the expected values better. For example, the Cauchy pressure ($C_{12} - C_{44}$) of Cantor alloy is close to 0. The results from the Lennard-Jones potential agree with this substantially more than the results from MEAM.

Next, for the polycrystalline case, the raw output stiffness tensor from the LAMMPS script for the system modelled with MEAM is:

$$C_{ij} = \begin{bmatrix} 246.2 & 127.1 & 124.0 & -1.2 & 7.7 & -3.3 \\ & 237.2 & 134.0 & -1.2 & -1.3 & 4.6 \\ & & 239.2 & -1.8 & -6.5 & -0.8 \\ & & & 56.4 & -0.9 & -1.3 \\ & & & & 46.4 & 3.2 \\ & & & & & 49.7 \end{bmatrix} \text{ GPa}$$

while the same system modelled with Lennard-Jones is:

$$C_{ij} = \begin{bmatrix} 282.1 & 94.4 & 89.5 & 5.1 & 12.8 & -5.9 \\ & 265.2 & 105.8 & -2.5 & -2.2 & 6.7 \\ & & 270.0 & -2.6 & -10.5 & -1.5 \\ & & & 88.0 & -1.7 & -2.1 \\ & & & & 71.5 & 5.1 \\ & & & & & 76.9 \end{bmatrix} \text{ GPa}$$

The Young's Modulus (E), bulk modulus (B), shear modulus (G), and Poisson's ratio (ν), calculated with Hill's averaging scheme, are shown in Tab. 5.4.

Table 5.4: MEAM vs. Lennard Jones: Polycrystalline Elastic Constant Results

	7 Grain MEAM	7 Grain Lennard-Jones
E / GPa	143.6	209.9
B / GPa	165.9	155.2
G / GPa	52.9	82.3
ν	0.356	0.275
CPU Hours	555.2	58.0

Interestingly, the Lennard-Jones potential better calculates the elastic constants than MEAM, even for polycrystalline cases. This is shown in Tab. 5.4, and the accuracy of the Lennard-Jones potential across a range of temperatures can be seen in Fig. 5.3. This is likely due to the fact that the Lennard-Jones potential was fit more to experimental values of elastic constants, while the MEAM used other material properties.

In Fig. 5.1, values of the 3 independent components of the stiffness tensor are plotted as a function of temperature. The results are compared to the experimental work of Teramoto et al. [39], the DFT results of Zaddach et al. [45], and the expected potential results from Gröger et al. [17]. It should be noted that only the results from Teramoto are across a range of temperatures, while the others are only simulations at 0K.

The Zener's anisotropy ratio is also plotted as a function of temperature, shown in Fig. 5.2a. Since an anisotropy value of 1 signifies an isotropic material, an increase of anisotropy can

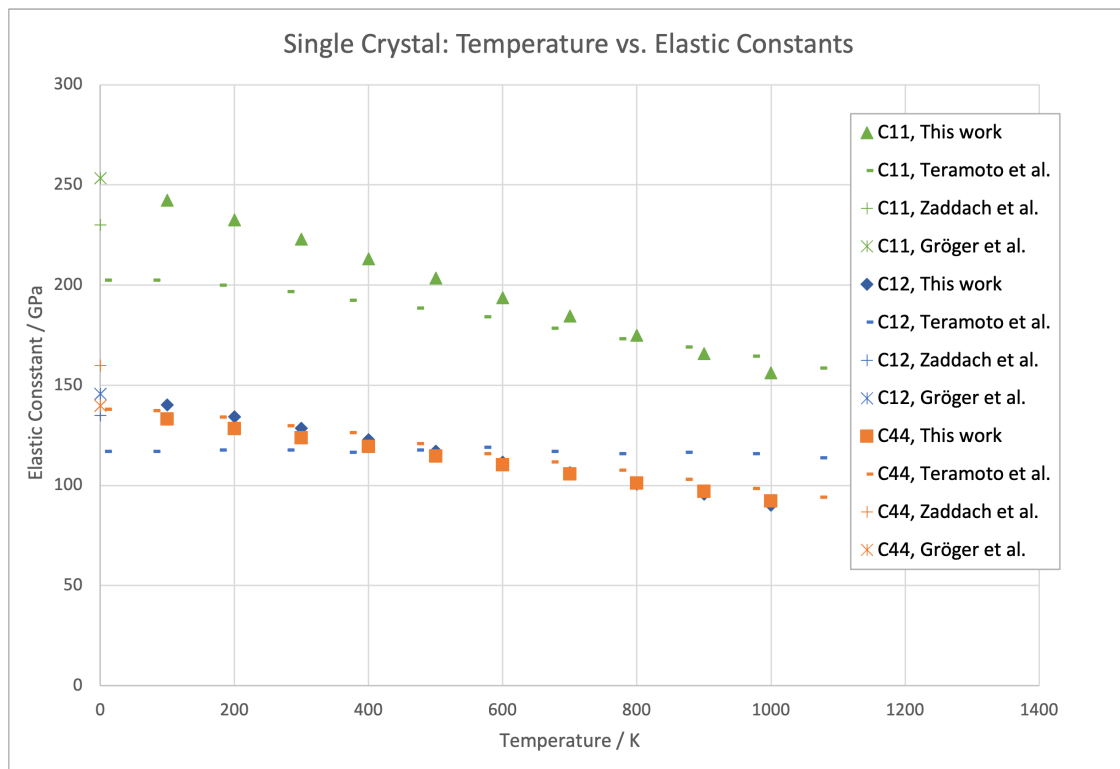


Figure 5.1: The monocrystalline elastic constants vs. temperature. This work is compared to the experimental work of Teramoto et al. [39], the DFT results of Zaddach et al. [45], and the expected potential results from Gröger et al. [17].

Table 5.5: Single Crystal: Temperature vs. C_{11}

Temp. / K	C_{11} , This work / GPa	C_{11} , Teramoto et al. / GPa
100	242.33	202.97
200	232.49	198.51
300	222.91	194.05
400	213.09	189.05
500	203.47	185.13
600	193.85	180.67
700	184.59	176.21
800	174.95	171.75
900	165.95	167.29
1000	156.16	162.83

Table 5.6: Single Crystal: Temperature vs. C_{12}

Temp. / K	C_{12} , This work / GPa	C_{12} , Teramoto et al. / GPa
100	140.2	118.0
200	134.2	117.7
300	128.5	117.3
400	122.9	116.9
500	117.1	116.6
600	111.6	116.2
700	106.3	115.8
800	100.5	115.4
900	95.6	115.1
1000	90.2	114.7

Table 5.7: Single Crystal: Temperature vs. C_{44}

Temp. / K	C_{44} , This work / GPa	C_{44} , Teramoto et al. / GPa
100	133.1	136.8
200	128.4	133.2
300	123.8	129.3
400	119.4	124.6
500	114.6	120.3
600	110.2	116.3
700	105.8	110.5
800	101.1	106.6
900	96.9	102.3
1000	92.1	97.6

be seen with increasing temperatures. The experimental results from Teramoto et al. [39] also follow the trend of increasing anisotropy with increasing temperature.

The directional dependence of the Young's modulus with regard to crystallographic orientation, shown in Fig. 5.2b, serves as an example and aid for visualizing the anisotropy. The darker regions further from the origin describe a larger modulus, while the areas closer to the origin and lighter in color describe a lower value. In this figure, the x, y, and z axis represent the [100], [010], and [001] crystallographic directions, respectively.

The last results from this section are the temperature dependence of a polycrystal with a grain size of ≈ 8.5 nm. In Fig. 5.3, the elastic moduli can be seen as a function of temperature, and are compared to the experimental works of Laplanche et al. [22] and Haglund et al. [47]. The simulated results of the Young's modulus and shear modulus, fit quite well to the experimental data, though there is a difference in the bulk modulus results at low temperatures of up to 23%.

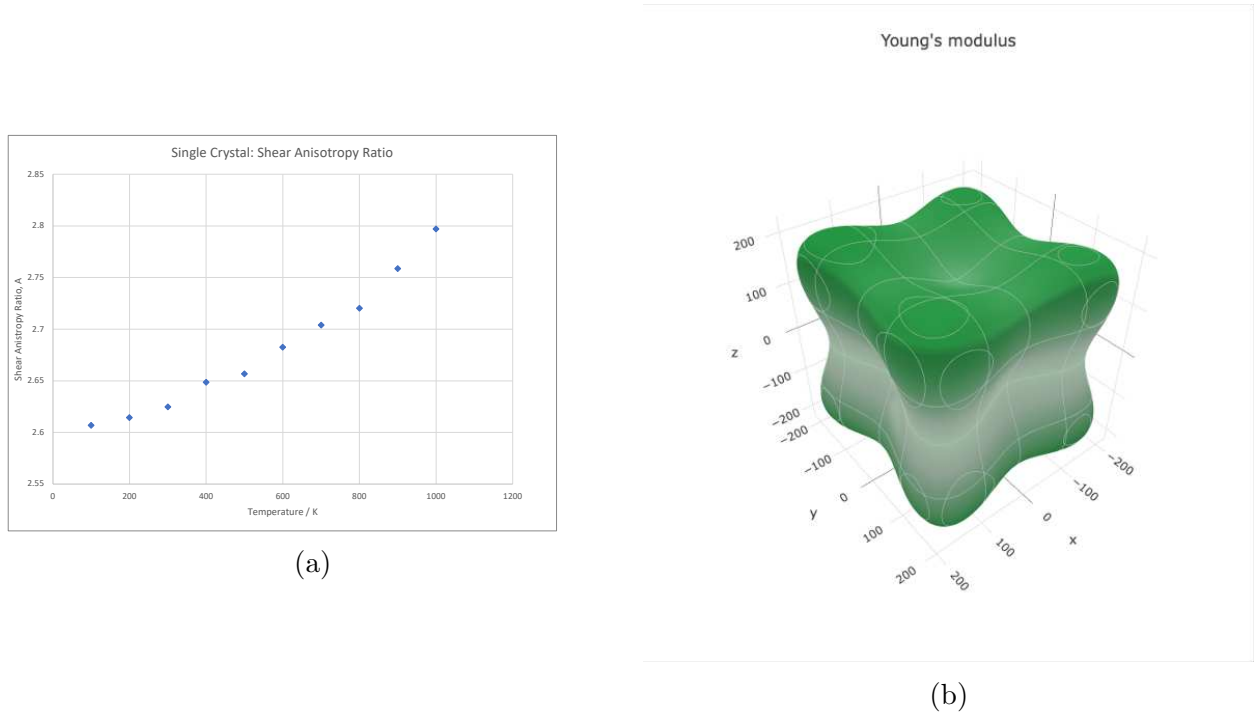


Figure 5.2: a) The Zener’s anisotropy ratio of a monocrystal compared to temperature. b) The directional dependence of the Young’s modulus, as visualized by Elate [46].

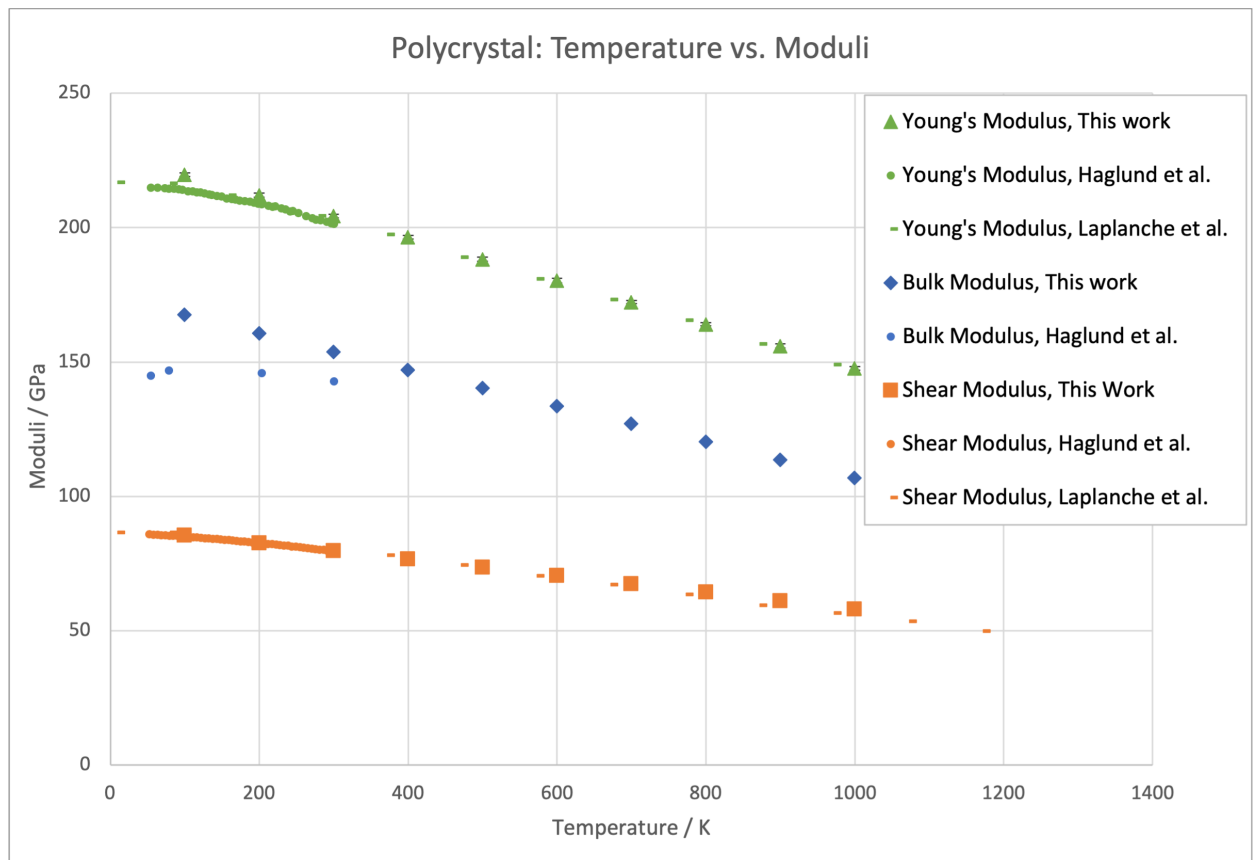


Figure 5.3: The polycrystalline elastic constants vs. temperature. This work is compared to the experimental works of Wu et al. [22] and Haglund et al. [47].

5.4 Discussion

The results of this chapter served to show that the potential is applicable across a range of temperatures, as well as to cement the fact that the elastic constants are correctly calculated in later chapters.

Especially for modelling an FCC metal with a pairwise potential, the monocrystalline elastic constants are quite well approximated. Comparing with the results from Gröger et al. [17], the methodology of this work was shown to be correct as it aligned well with the results from Gröger. As many or all properties of a modelled material will change when the potential is changed even slightly, it is impossible to isolate and better fit only certain properties to experiment, as described by Gröger. The other two independent constants, C_{12} and C_{44} , are better approximated, but an acceptable amount of error still exists.

This error in the slope of the C_{12} values is likely an effect of the Lennard-Jones potential. As discussed previously, pairwise potentials such as the Lennard-Jones have a Cauchy pressure of 0. It is likely that this potential was fit to more closely match the C_{44} values or a property dependent more on C_{44} than C_{12} , leading to the C_{44} values more closely matching experimental results. It is important to note that a pairwise potential could not perfectly match both C_{44} and C_{12} , if they have different slopes.

For the polycrystalline simulations, the potential, and model used fits the experimental results even better. For the Young's modulus and shear modulus in Fig. 5.3, the resulting values are very much in agreement with the experimental results. There is still some error in the bulk modulus at very low and very high temperatures. This is speculated to be an issue similar to the C_{11} error in Fig. 5.1, where it is only an effect from the limitations of fitting a Lennard-Jones potential to different material properties.

In the next chapter, the polycrystalline cases will be examined as a function of grain size rather than temperature.

Influence of Grain Size on Elastic Constants

6.1 Motivation

The influence of grain size on elastic constants has been measured for many materials, including the FCC metals Fe [48], Cu [49], and Pd [48]. The results all show a significant decrease in elastic constants of about 20% when grain sizes decrease from around 10-20 nm [50]. For all materials, it is important to understand how the microstructure affects the mechanical properties in order to better tune the material to the application.

This relationship has been measured for other medium entropy alloys [51] and high entropy alloys [52], but has not yet been sufficiently studied for Cantor alloy. This was the earliest inspiration for this project.

6.2 Simulation

The simulation plan for the grain size vs. elastic constants is shown below in Tab. 6.1. This range of grain sizes was chosen as it is the range found to have degrading mechanical properties in other FCC metals. Each of the tests were generated and equilibrated at 300K as described in Chapter 3. The stiffness tensor and resulting moduli were calculated as described in Chapter 2 through the LAMMPS example script and Hill's averaging method.

The exact parameters for these simulations were the same as for Chapter 5, and can be seen in Tab. 5.2.

Table 6.1: Simulation plan for grain size vs. elastic constants

Number of Grains	Grain Size in nm	Number of Trials
1	20.00	6
2	15.87	6
4	12.60	6
7	10.46	6
10	9.28	6
13	8.51	6
16	7.94	6
19	7.50	6
31	6.37	6
120	4.05	6

6.3 Results

A significant change in the slope of the curve at about 8 nm can be seen in each of the plots with grain size as the independent variable. This can be seen specifically in grain volume fraction in Fig. 6.3b, Young's modulus, shear modulus, bulk modulus, and Poisson's ratio vs. grain size in Fig. 6.2 and Tab. 6.2. There is a 30% increase in Young's modulus from 4 nm grains to 20 nm grains. There is also a 30% increase in the shear modulus, while the bulk modulus only increases by about 8%.

Table 6.2: Predicted polycrystalline elastic properties

Grain Size / nm	E / GPa	G / GPa	K / GPa	Grain Boundary Volume Fraction
20.00	230.73	91.58	160.04	1.5
15.87	221.53	87.48	157.82	2.2
12.60	215.54	84.83	156.43	3.2
10.46	209.96	82.37	155.18	4.0
9.28	206.62	80.90	154.38	4.6
8.51	204.33	79.89	153.93	4.9
7.94	202.17	78.94	153.46	5.2
7.50	200.55	78.24	153.01	5.5
6.37	194.77	75.72	151.7	6.4
4.05	175.33	67.32	147.72	9.8

Fig. 6.3b shows the grain boundary volume fraction. More specifically, this figure shows the inverse percentage of atoms in an FCC structure out of the total atoms in the system, calculated with Ovito [38]. As expected, as grain size increases, the grain boundary volume fraction decreases since more atoms are in the bulk of the grains in the FCC structure.

Since the grain boundary percentage and many of the elastic properties seem to follow a similar trend, only inverted, it was thought to compare the elastic constants as a function of grain boundary volume fraction. This is shown in Fig. 6.4d, where the relationship is seen

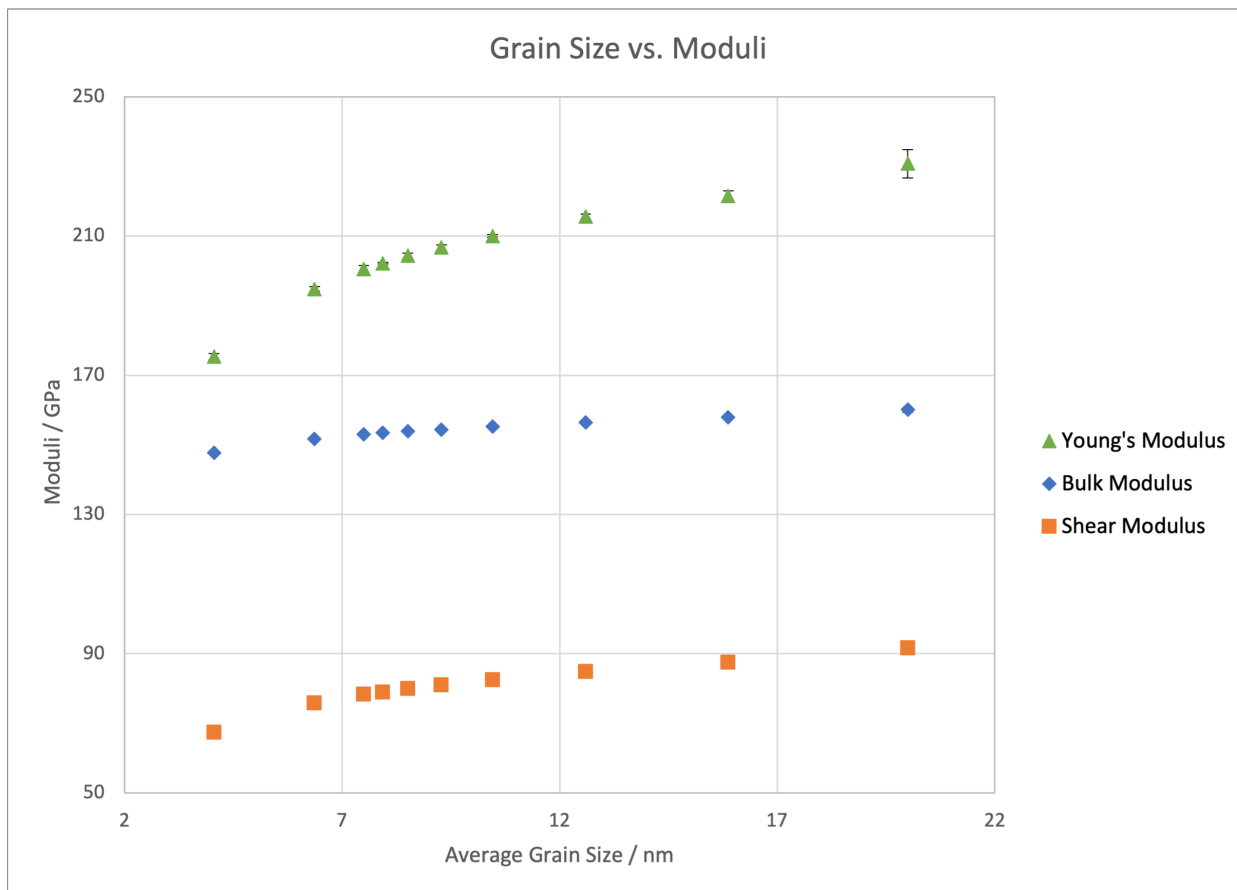


Figure 6.1: The polycrystalline elastic constants vs. grain size.

to be nearly linear. From this, it can be concluded that the change in elastic constants due to grain size is more directly due to the change in volume fraction of the atoms in the grain boundaries, than to the actual change in size of the grain itself.

6.4 Discussion

The results from this chapter are similar and in agreement with the results of other FCC metals [50] and medium entropy alloys [51]. The elastic constants are increasing with grain size across the range, though there is a transition point around 8 nm where any additional increase in grain size has less of an effect than before. This transition in values around 8 nm is also found in the medium entropy alloy CoCrNi [51], and at slightly larger grain sizes in other FCC metals [50]. Zhang et al. [51] speculates that at below 8 nm grain size the additional atoms in the grains have a substantial effect on the material properties, but for grain sizes larger than 8 nm the additional atoms have a lesser effect. This transition point may be geometry-based or defect-based, but there is clearly a transition point where the microstructure and the way atoms are distributed starts to have a different influence on the mechanical properties.

6.4 Discussion

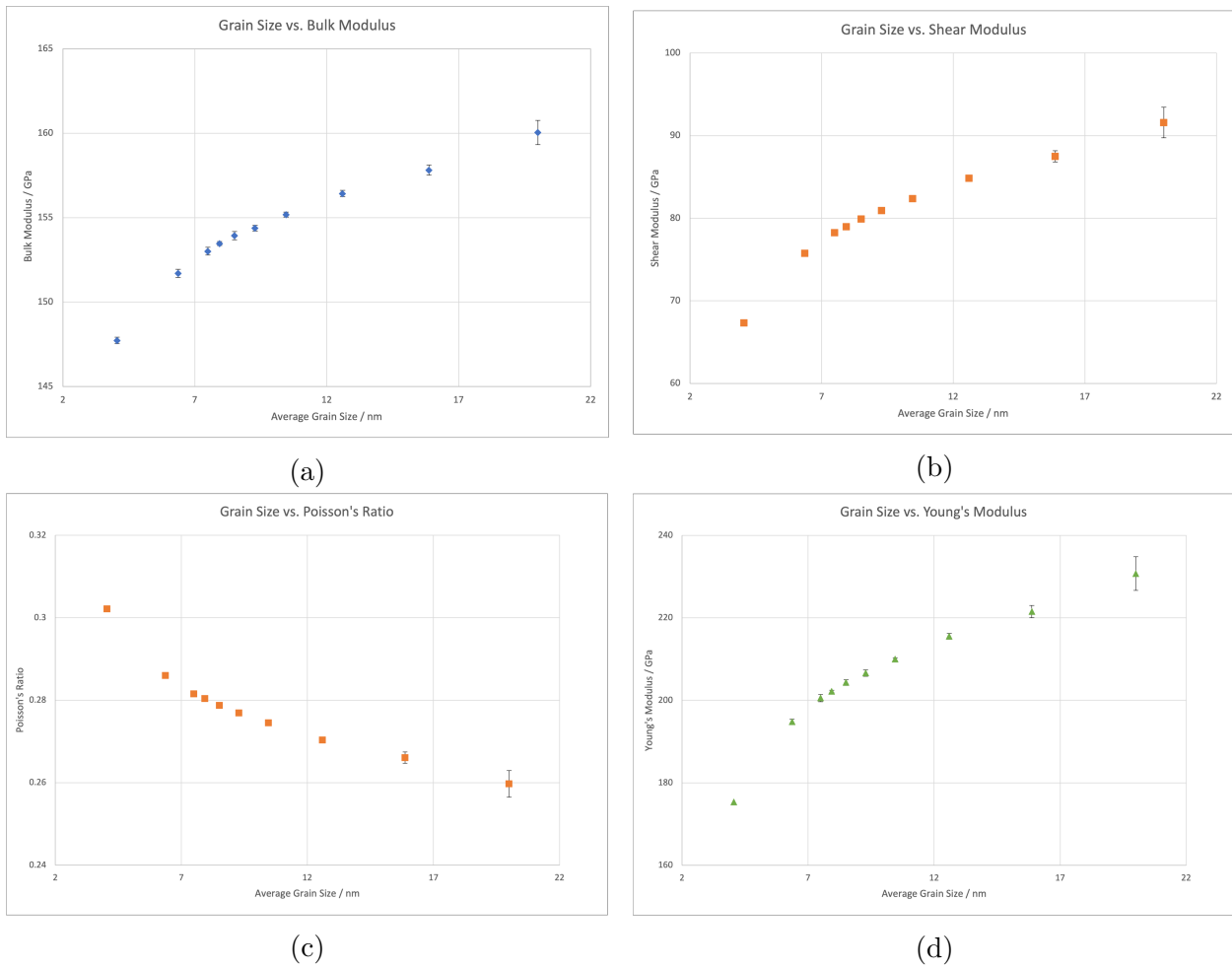


Figure 6.2: The elastic moduli as functions of grain size. a) The bulk modulus as a function of grain size. b) The shear modulus vs. grain size. c) The Poisson ratio as a function of grain size. d) The Young's modulus vs. grain size.

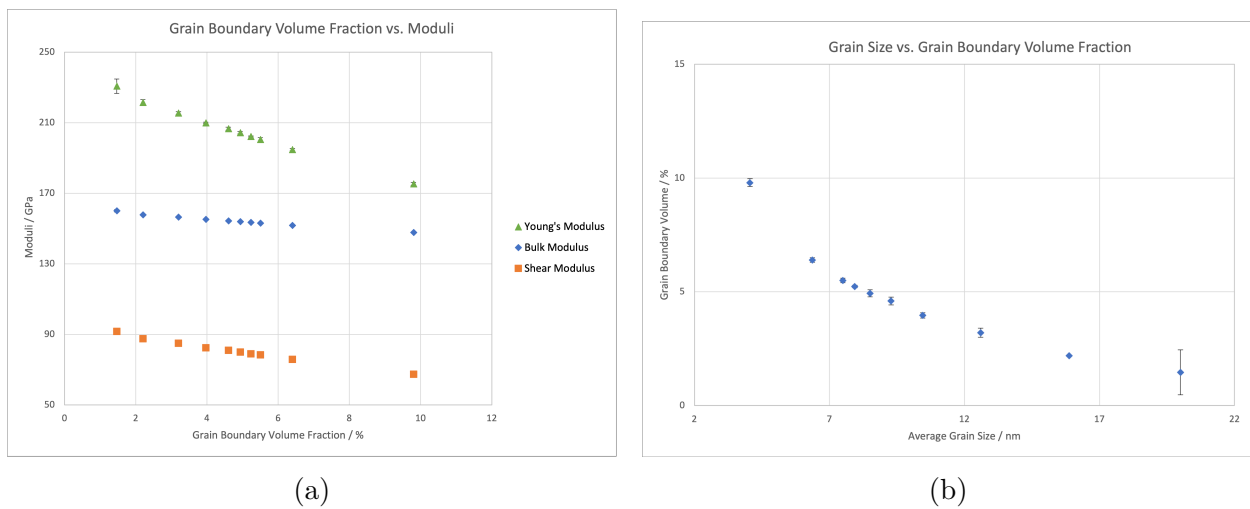


Figure 6.3: a) The grain boundary volume fraction vs. elastic constants. b) The percentage of atoms in grain boundaries compared to grain size.

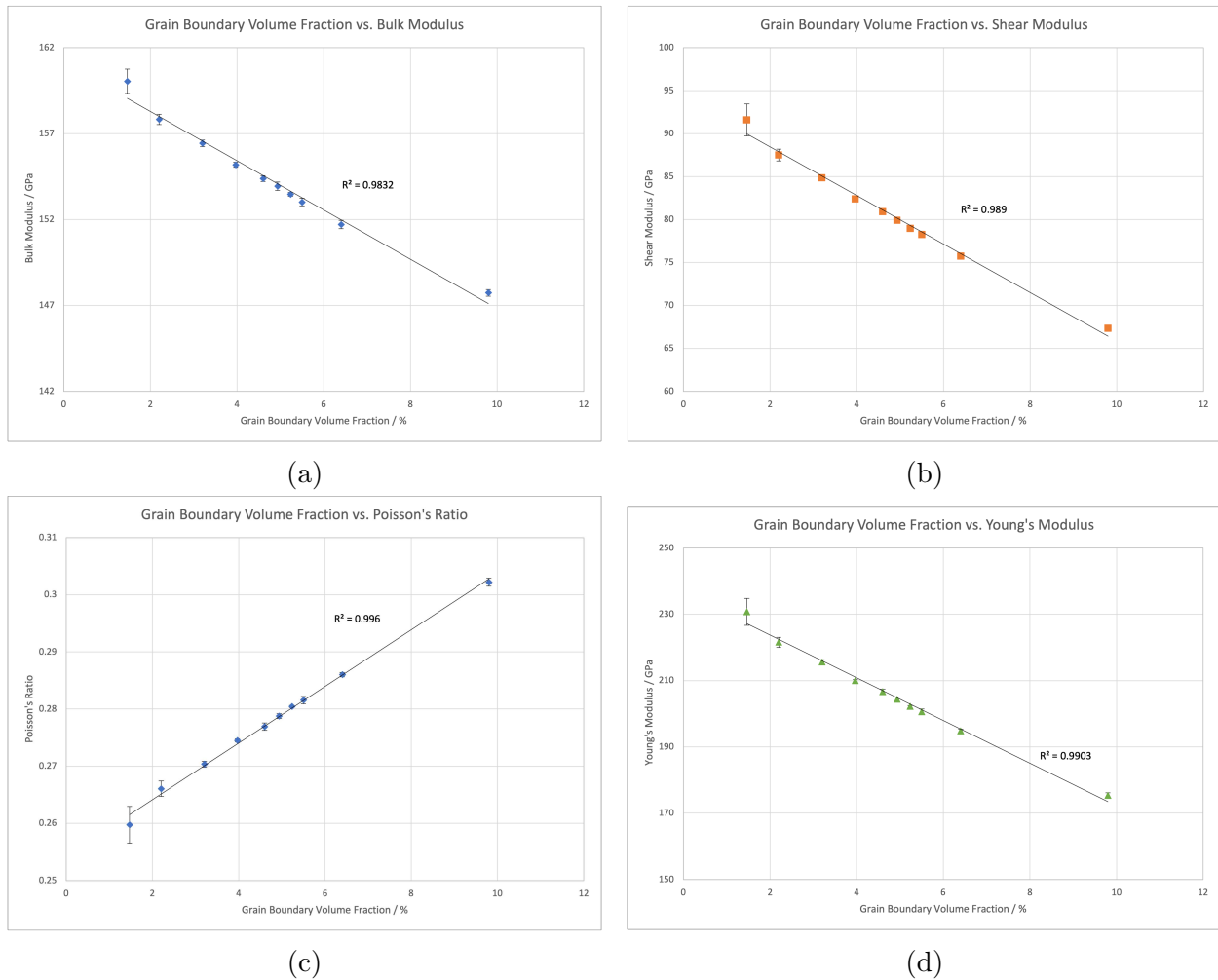


Figure 6.4: The elastic moduli as functions of the grain boundary volume fraction. a) The bulk modulus as a function of grain boundary volume fraction. b) The shear modulus vs. grain boundary volume fraction. c) The Poisson's ratio as a function of grain boundary volume fraction. d) The Young's modulus vs. grain boundary volume fraction.

Interestingly, this distinct change in slope also occurs in the grain boundary volume fraction curve, shown in Fig. 6.3b. It can then be inferred that the elastic constants vary more linearly with grain boundary volume fraction than with grain size. This point is further backed up in Fig. 6.4, where the relationship of each elastic constant is linear with the grain volume fraction.

Looking forward, it would be interesting to analyze larger and smaller grain volume fractions in order to see if this trend continues over a wider range of grain sizes.

Nanoindentation

7.1 Motivation

In Chapters 5 and 6, the effect of temperature and grain size on elastic constants was discussed. It has been shown that the yield strength, hardness, and creep of metals is also dependent on temperature [53] and grain size [54, 55]. The relationship of hardness to temperature is quite as expected: hardness decreases with increasing temperature. While dislocations have a higher drag coefficient at higher temperatures [56, 57], there are also many temperature effects which promote dislocation glide. Firstly, at higher temperatures a lower Peierls stress is measured [58], meaning that the energy boundary to initiate plastic deformation is lower. Additionally, temperature can activate dislocation sources and even change the movement to perpendicular to the dislocation's glide plane, called dislocation climb. Lower energy barriers for dislocation movement combined with a lengthening of the interatomic bonds due to the increase in thermal energy leads to a decrease in the strength, hardness, and elastic moduli of the metal.

The temperature effects on the hardness of the Cantor alloy have not been extensively studied, either experimentally or through simulation.

The effect of grain size on the hardness of metals is slightly more complicated. At the microscale, hardness has been found to increase with inverse grain size, often referred to as grain boundary strengthening. This is known as the Hall-Petch relationship [59, 60], where the yield stress and hardness for metals are found to increase linearly with the square root of decreasing grain size. This is shown in Eq. 7.1

$$\sigma = \sigma_0 + kd^{-\frac{1}{2}} \quad (7.1)$$

where σ is the yield stress, σ_0 is the yield stress of a single crystal, k is a measure of the local stress needed to initiate plastic deformation at a grain boundary or the flow stress, and d is the average grain size [61].

On the nanoscale, while some metals follow the Hall-Petch relationship [55, 62], others are shown to do the opposite, known as the inverse Hall-Petch relationship, or grain boundary weakening. The inverse Hall-Petch occurs because there is a point where the main mechanism for plastic deformation is grain boundary sliding or rotation, in contrast to mainly dislocation glide [61]. This means that on the nanoscale, the hardness of some metals increases with increasing grain size. This has been observed experimentally [63] and through simulation [64–67].

For grain sizes on the microscale, the Hall-Petch relationship has been measured experimentally for Cantor alloy in the work of Liu et al. [68], and evidence for the inverse Hall-Petch relationship has been found on the nanoscale regarding the wear resistance of Cantor alloy [69]. Furthermore, a recent MD study from Zhang et al. [67], on a different HEA, shows the inverse Hall-Petch region, the Hall-Petch region, as well as the transition zone with maximum hardness.

The main motivation of this section is to corroborate if Cantor alloy shows an inverse Hall-Petch relationship, and to calculate the maximum hardness as well as the grain size at which it occurs.

7.2 Simulation

The script for nanoindentation was taken partly from the PhD. thesis of Lukas Löfler [70] and partly from the LAMMPS documentation. The steps are as follows:

1. Equilibrate systems as described in Chapter 3
2. Equilibrate systems with new boundary conditions (indentation axis cannot be periodic)
3. Indent material
4. Hold indenter at maximum defined depth
5. Remove indenter
6. Calculate residual imprint area

A visual of this procedure can be seen in Figs. 7.1, 7.2, and 7.3, showing a schematic of the simulation setup as well as a monocrystal after indentation.

It is important to note that the previously equilibrated systems must be equilibrated again due to changing boundary conditions. The indent script in LAMMPS requires a non-periodic

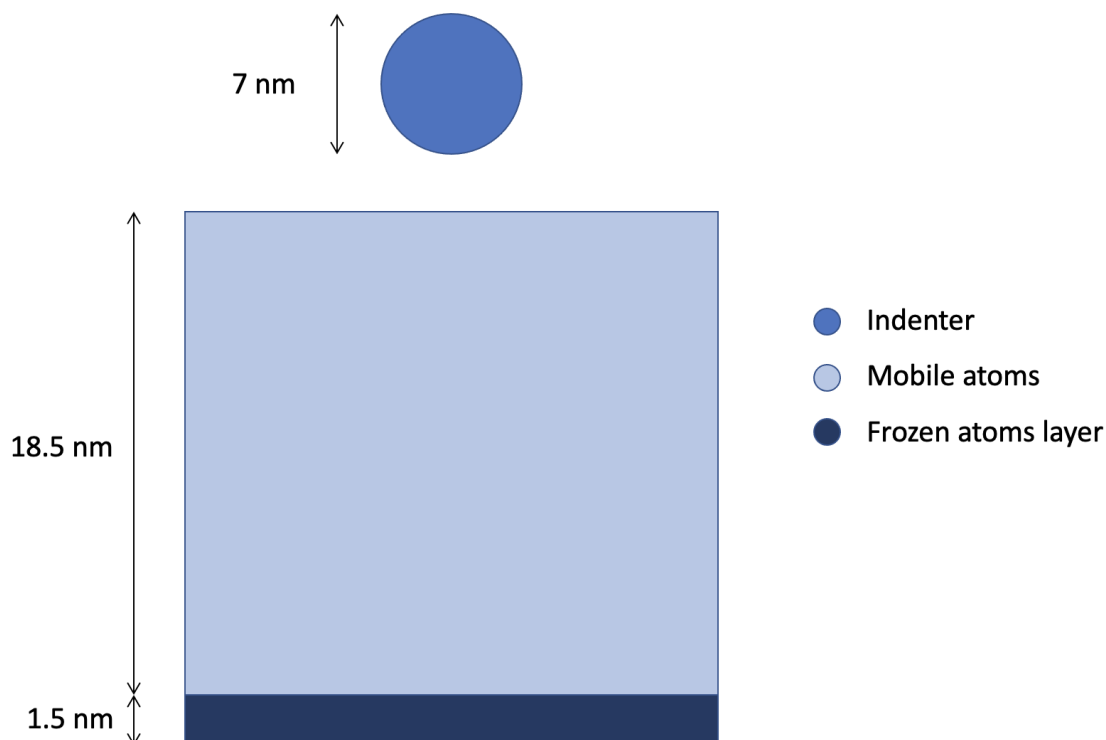


Figure 7.1: A schematic showing the simulation setup. An indenter of radius 3.5 nm can be seen along with a frozen layer of atoms at the bottom of the simulation box. The atoms in the middle are fully mobile.

boundary in the direction of indentation, as this would lead to obvious issues. In order to deal with the non-periodic boundary, a simple solution is to freeze a layer of atoms at the bottom of the simulation. This prevents atoms from being pushed through or extending the boundary, but does not allow the material to act as a bulk. Also shown in Fig. 7.1 is the indenter invoked by the `fix indent` command and the mobile atoms in the middle. The mobile atoms are only controlled by an NVE ensemble and the `temp/rescale` command in LAMMPS. This was chosen over the typical NpT ensemble because the x-y area, and thus the area between indentations and relative area of indentation, should be consistent between simulations.

The force between the indenter and each atom in the material is described as

$$F(r) = \begin{cases} -k(r - R)^2 & \text{if } r \leq R \\ 0 & \text{if } r > R \end{cases} \quad (7.2)$$

where $F(r)$ is the repulsive force between the indenter and the simulated particles, k is a user-defined constant, r is the radial distance from an affected particle to the center of the indenter, and R is the radius of the indenter. The direction of this force is perpendicular

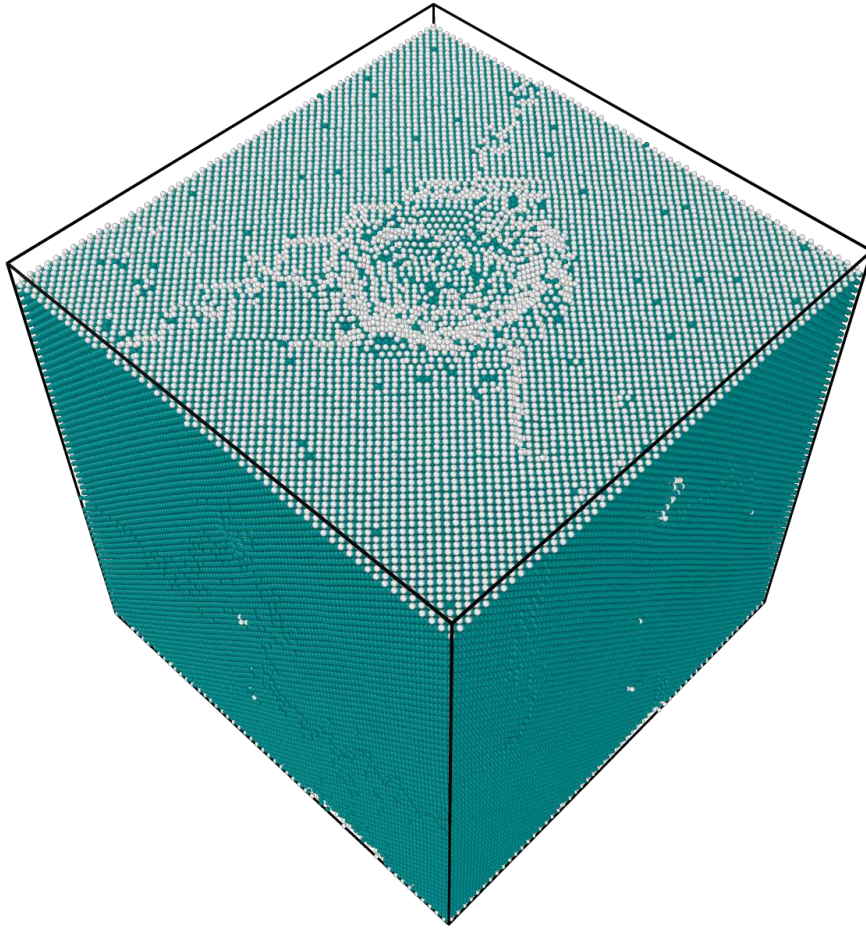


Figure 7.2: A snapshot of the nanoindentation simulation. Shown is a monocrystal with plastic deformation around the indenter tip.

to the sphere's surface. This allows the user to define the interactions between the tip and surface atoms very easily, without worrying about attractive forces.

Once the indentation, hold, and removal steps are complete, the data must be analyzed. Using Eq. 2.23, the hardness can be calculated with the average maximum force at the maximum indentation depth and the resulting area of the imprint after the indenter is removed.

To calculate F_{max} , the average force in the z-direction during the hold step was used. This was done to remove any velocity or inertia effects during the rapid indentation speeds during MD nanoindentation.

For nanoindentation at the atomic scale, care must be taken to calculate the area properly. As described by Ziegenhain et al. [71], the area should be calculated using the center atom coordinates of the atoms contacted by the indenter. This leads to an elliptical area equation:

$$A_{ellipse} = \frac{\pi}{4}[(x_{max} - x_{min})(y_{max} - y_{min})] \quad (7.3)$$

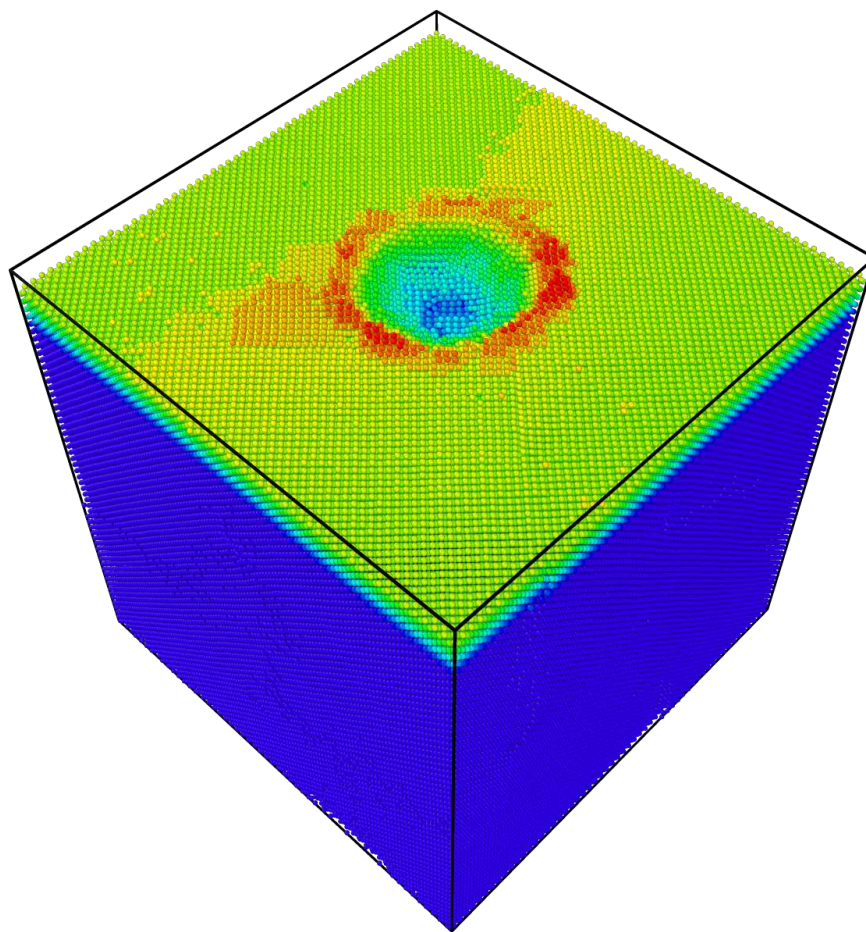


Figure 7.3: A snapshot of the nanoindentation simulation. Pile-up can clearly be seen around the edges of the indented area.

where x and y are the coordinates of the furthest atoms contacted by the indenter. This is most necessary at very low indentation depths or with very small indenters, where the scale is similar to the lattice constant. In this work, both the contact area and indenter are an order of magnitude larger than the lattice constant, so this was approximated for simplicity. In addition, this work only focuses on a maximum hardness value, while the equation described by Ziegenhain is useful for continuous hardness measurements.

In this work, the area was approximated as

$$A = \pi(r_{area})^2 \quad (7.4)$$

where r_{area} is the radius of the circle projected onto the surface of the contact area from the indenter. r_{area} was calculated using the geometry of the simulation, and can be calculated as a function of the indentation depth. During the removal of the indenter, there is a point at which the force returns to zero. It is at this point that the relaxed indentation area was calculated. These points can be seen in Figs. 7.4 and 7.5.

Both the influences of temperature and grain size on the force/displacement curves and

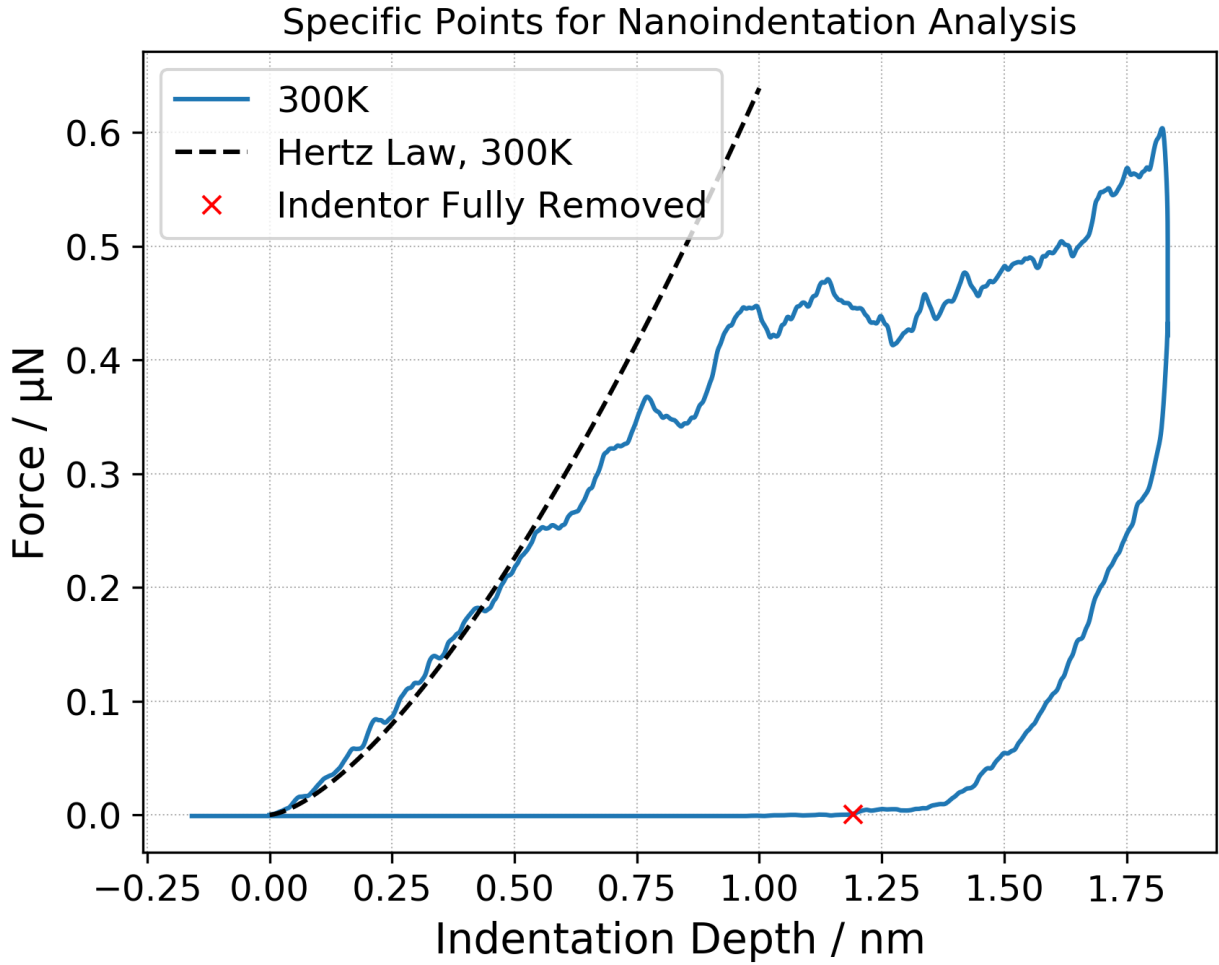


Figure 7.4: An example force/displacement curve during nanoindentation. Shown is the point during the removal of the indenter at which the force returns to zero. This depth was used in Eq. 7.4 to calculate the residual area after indentation.

hardness were to be calculated. An overview of the trials runs is shown in Tab. 7.1 and 7.2, and the specific test parameters used are shown in Tab. 7.3.

As seen in 7.4, the force vs. displacement curves for the single crystals were compared to Hertz contact theory or Hertz Law [72]. Hertz contact theory relates the elastic response to the compressive force between two spherical solids, or one spherical and one flat surface. While Hertz Law was derived in the late 1800s, it was not widely used until nearly a century later. Currently, Hertz contact theory is used primarily for nanoindentation purposes, including measuring changes in contact radius [73], validating nanoindentation simulations [74, 75], and AFM nanoindentation [76].

Hertz Law states that for two frictionless and purely elastic solids, the applied force F can be related to the elastic properties of the materials through Eqn. 7.5:

$$F = \frac{4}{3}E^*\sqrt{Rh} \quad (7.5)$$

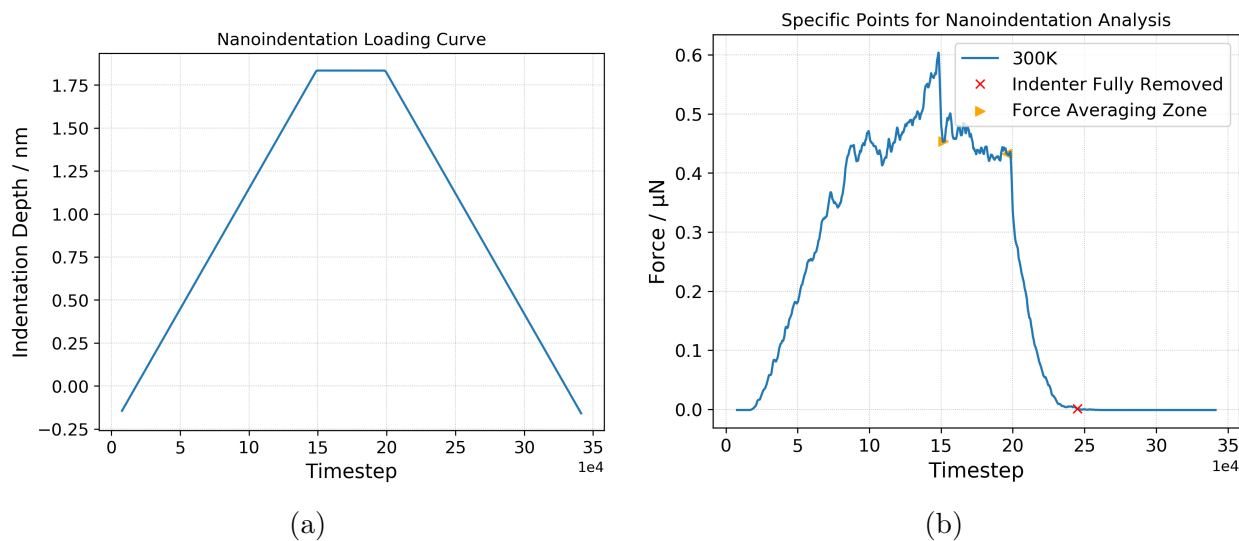


Figure 7.5: a) The position of the indenter plotted as a function of timestep. b) An example force vs. timestep curve during nanoindentation. The values in the averaging zone occurred during the holding of the indenter, and were averaged and used in Eq. 2.23 to calculate the hardness.

Table 7.1: Simulation Plan for Nanoindentation vs. Temperature

Test	Temperature / K	Grain Size / nm
1	100	Aligned single-crystal, 20
2	200	Aligned single-crystal, 20
3	300	Aligned single-crystal, 20
4	400	Aligned single-crystal, 20
5	500	Aligned single-crystal, 20
6	600	Aligned single-crystal, 20
7	700	Aligned single-crystal, 20
8	800	Aligned single-crystal, 20
9	900	Aligned single-crystal, 20
10	1000	Aligned single-crystal, 20

Table 7.2: Simulation Plan for Nanoindentation vs. Grain Size

Number of Grains	Temperature / K	Grain Size / nm
1	300	20.00
2	300	15.87
4	300	12.60
7	300	10.46
10	300	9.28
13	300	8.51
16	300	7.94
19	300	7.50
31	300	6.37
120	300	4.05

Table 7.3: Parameters for Nanoindentation

Parameter / Units	Value
Timestep / fs	0.1
Indenter velocity / $\frac{m}{s}$	140
Force constant k from Eq. 7.2	1

where E^* is the reduced modulus, R is the radius of curvature, and h is the indentation depth. The reduced modulus, E^* , can be calculated by:

$$\frac{1}{E^*} = \frac{1 - \nu_1^2}{E_1} + \frac{1 - \nu_2^2}{E_2} \quad (7.6)$$

where E_1 and E_2 are the Young's moduli of the contacting materials, and ν_1 and ν_2 are the Poisson's ratios of the contacting materials. In the simulations conducted in this work, the Young's modulus of the spherical indenter is infinite, so the equation simplifies to:

$$\frac{1}{E^*} = \frac{1 - \nu_s^2}{E_s} \quad (7.7)$$

where E_s and ν_s are the Young's modulus and Poisson's ratio of the indented material, respectively.

Using the elastic constants calculated in Chapter 4, Hertz contact theory was used to validate the simulation results in the elastic region of the force vs. displacement curves.

7.3 Results

Typically, hardness, yield stress, or flow stress are used to describe the stresses during plastic deformation. In this work, both the hardness values and the force/displacement curves are displayed. The results of Fig. 7.6 and 7.9a show a significant temperature dependence of both the plastic and elastic response during nanoindentation, respectively. In the elastic region, the simulated results align quite well with Hertz contact theory using elastic data from Chapter 6, shown in Fig. 7.9a.

The results in Fig. 7.7 show a clear decreasing trend of hardness with increasing temperature. This follows the theory described in the motivation: higher temperature in metals usually leads to lower hardness and yield strength due to easier dislocation motion and therefore a lower flow stress and hardness. However, while the trend is correct, the simulated values differ from experiment. In experiment, hardness values range from 100 to 200 HV, or 1 to 2 GPa [68, 77]. The simulated results are an order of magnitude higher, with values of approximately 10 to 20 GPa. Presently, there is no explanation for this discrepancy.

The effects of grain size cannot only be seen clearly in the elastic region, shown in Fig. 7.9b, but also in the plastic region, shown in Fig. 7.8.

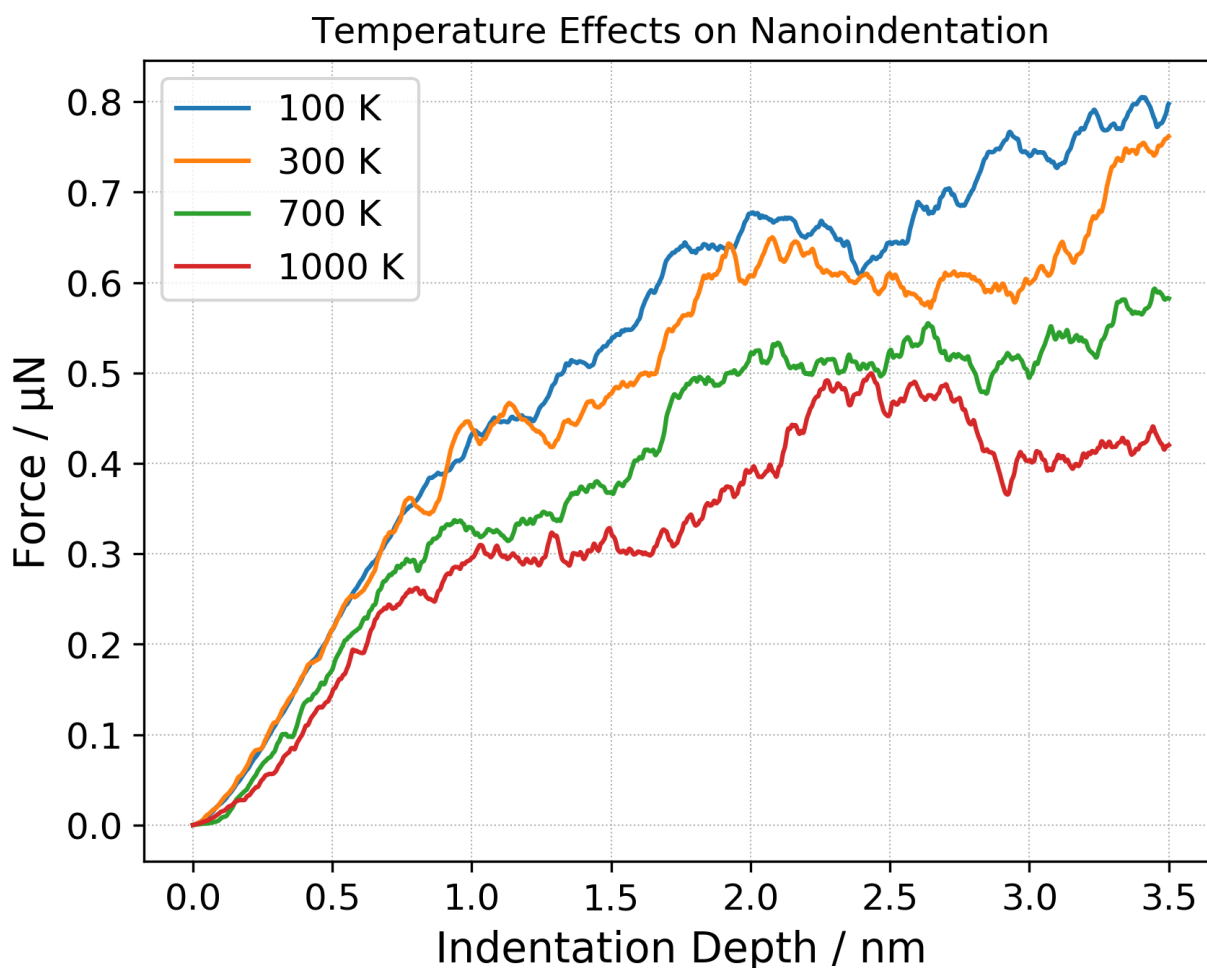


Figure 7.6: The influence of temperature on the force/displacement curves. The simulations shown are the aligned monocrystals.

A clear inverse Hall-Petch relationship can be seen. The hardness values in Fig. 7.10 increase from 11.3 GPa at 4 nm grain sizes to 17.2 GPa at 20 nm grain sizes, over a 50% increase.

7.4 Discussion

Once again, the first section of this chapter served primarily to confirm the methodology of the simulation steps to yield useful, meaningful, and realistic results. The calculated hardness values were higher than experimental values, pointing towards errors during plastic deformation. The difference between the experimental values and the simulated values is likely due to the difference in indentation speeds. The simulated nanoindentation results of Lu et al. [74] show a trend of increasing calculated hardness with increasing indentation speed. For the amount of simulations ran, it was speculated that running at faster indentation speed but then using the force during which the indenter position was held constant, would minimize the effects of higher velocity. While this did lessen the effects, the calcu-

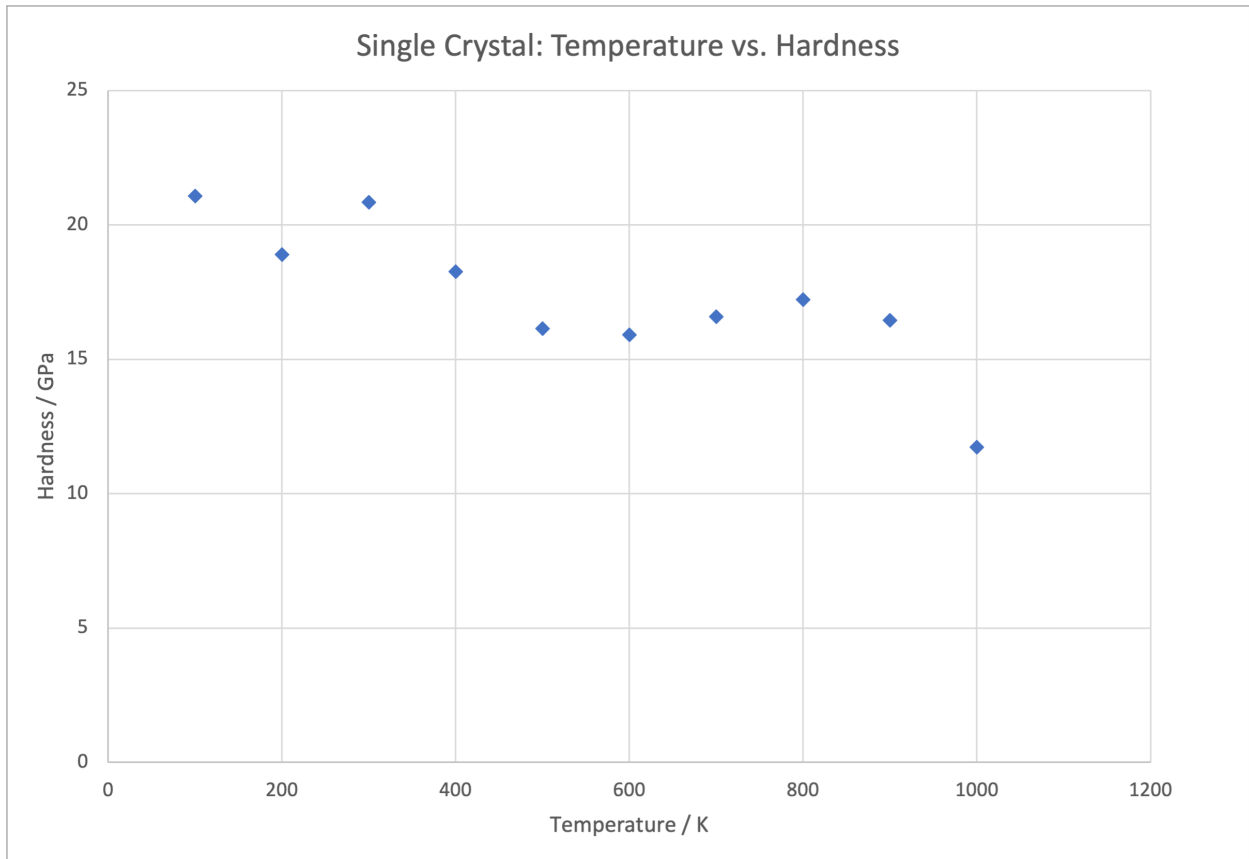


Figure 7.7: The influence of temperature on the calculated hardness values. The simulations shown are the aligned monocystals.

Table 7.4: Single Crystal: Temperature vs. Hardness

Temperature / Kelvin	Hardness / GPa
100	21.1
200	18.9
300	20.8
400	18.3
500	16.2
600	15.9
700	16.9
800	17.2
900	16.5
1000	11.7

lated hardness was still too high, and it would be of interest to run similar experiments at much lower indentation speeds. Interestingly, while the final hardness values differ from experiment, the force vs. displacement curves in Fig. 7.9a match the theoretical curves from Hertz Law. Therefore, the methodology used to simulate nanoindentation is shown to yield useful and realistic values, at least during low indentation depths in the elastic region. At

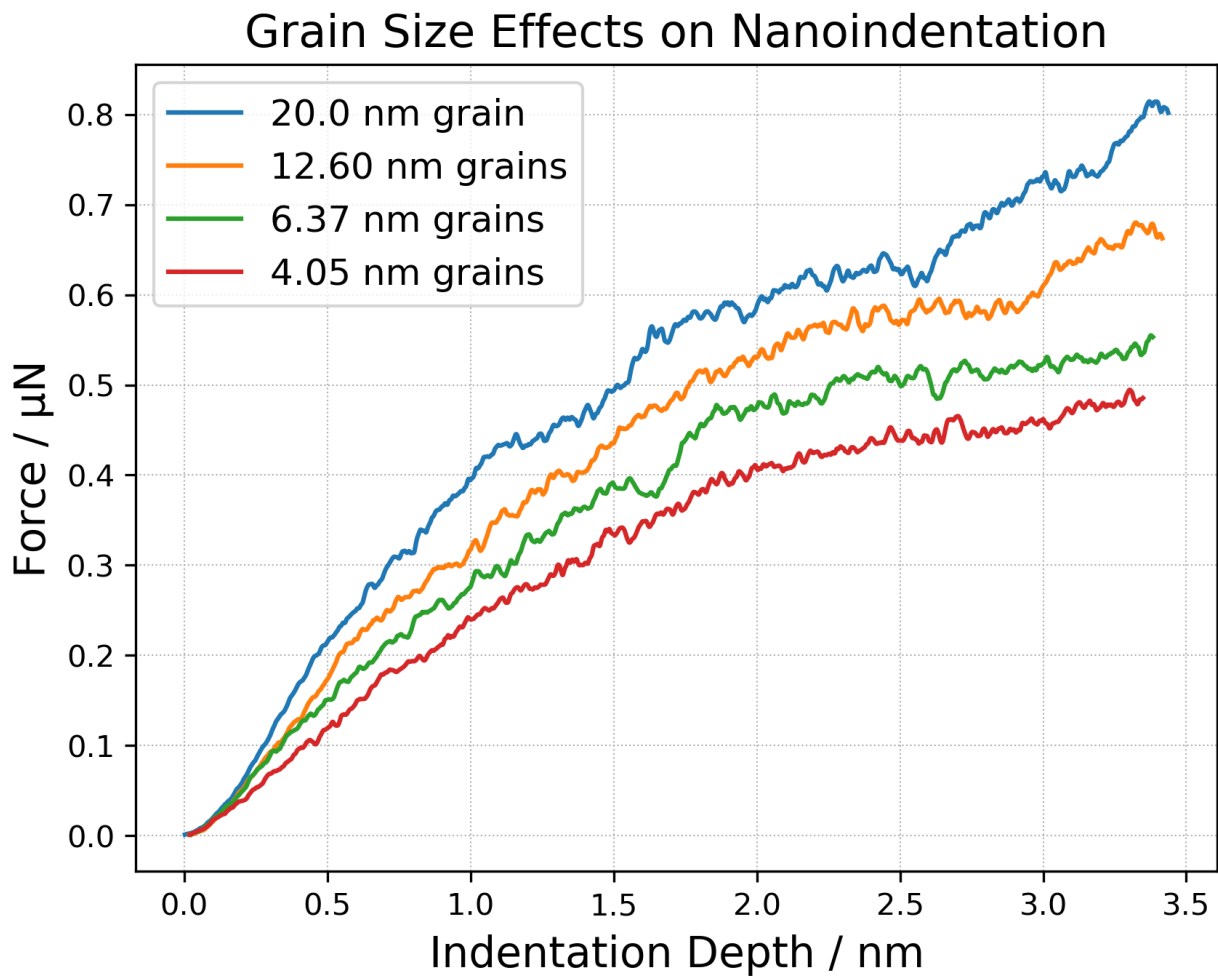


Figure 7.8: The influence of grain size on the force/displacement curves.

low indentation depths, the force is theoretically only a function of the elastic moduli, and the temperature dependence of elastic moduli was confirmed in Chapter 5.

For the hardness values shown in Fig. 7.7 and therefore higher indentation depths with plastic deformation, the expected trend of decreasing hardness with increasing temperature can be seen. The flow stresses shown in Fig. 7.6 back up these results as a clear difference can be seen.

The grain size vs. hardness results are at least as clear and distinct as the temperature vs. hardness results. At both low and high indentation depths, a clear difference in the force vs. displacement curves can be seen in Figs. 7.9b and 7.8, respectively. This shows both the grain size dependence on elastic modulus and flow stress. An inverse Hall-Petch relationship can be seen in Fig. 7.10. The transition point from the inverse Hall-Petch to the regular Hall-Petch relationship occurs at grain sizes larger than 20 nm, and therefore could not be seen in this work. But there is a critical grain size that leads to maximum hardness for the Cantor alloy.

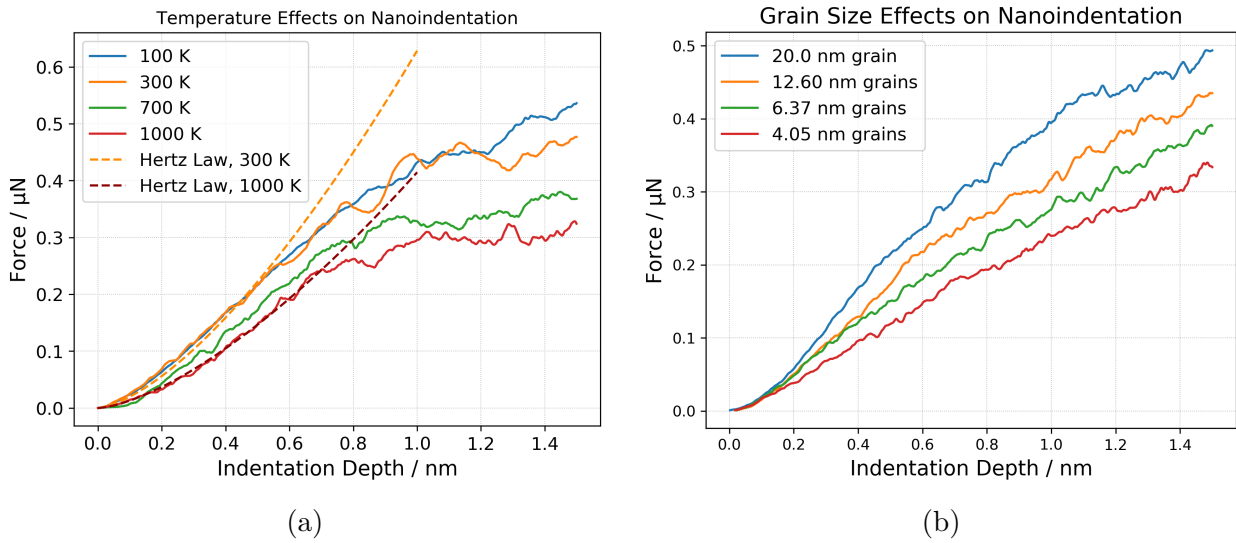


Figure 7.9: a) The influence of temperature on the force/displacement curves. b) The influence of grain size on the force/displacement curves. The data is equivalent to that of Fig. 7.6 and 7.8, but shows lower indentation depths in more detail.

For future work, it would be of interest to run a series of experiments with larger simulation box size to find this transition point. It is expected that the results would look similar to the results of Zhang et al. [67]. Once the transition point is found through simulation, it can be confirmed by experiment. Since annealing is a very time-consuming procedure, time and resources can be saved by finding the theoretical transition point through simulation before turning to experiment.

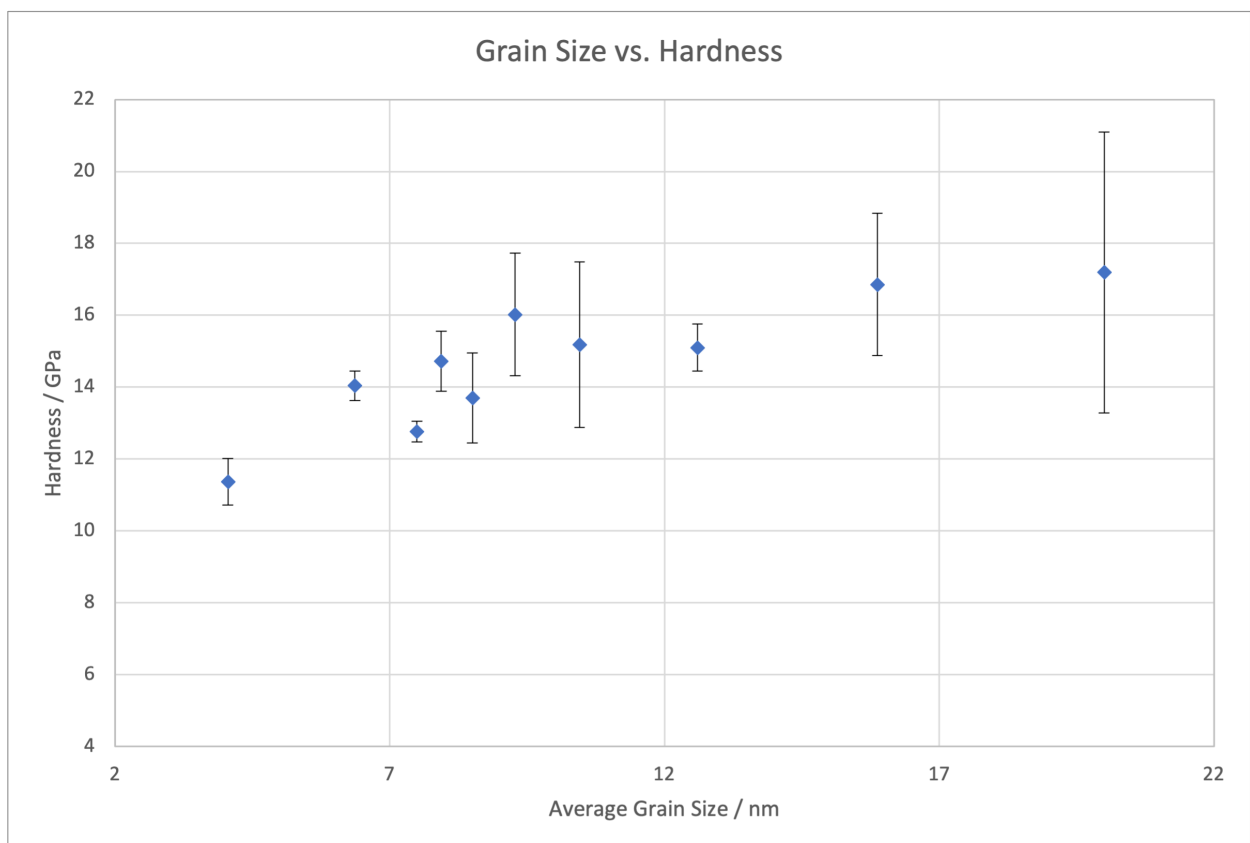


Figure 7.10: The influence of temperature on the calculated hardness values. The simulations shown were conducted at 300 K.

Summary

In this work, several simulations were conducted on the high entropy alloy CoCrFeMnNi, or Cantor alloy, using molecular dynamics methods. The linear coefficient of thermal expansion, elastic constants, and hardness through nanoindentation were calculated. Using molecular dynamics rather than DFT for these simulations allowed grain sizes up to 20 nm to be investigated, impossible with DFT. In addition, this work showed the usability of a pairwise potential for HEAs for polycrystalline systems by comparing results to experiment. New results were also investigated in ways not yet conducted experimentally.

Fully equilibrating a polycrystalline system with lattice distortion proved to be quite difficult, though through deliberate equilibration steps the systems were equilibrated. The volume difference between the same simulations equilibrated at different temperatures was used to calculate the linear CTE at each temperature.

As shown in Chapter 4, the polycrystalline linear CTE was found to be reasonably similar to experimental results, showing the usability of the pairwise potential for polycrystalline HEAs.

The elastic constant results across a range of temperatures were measured and proved to be within expected values from experiment and DFT. Here, no new information was found, but rather the methodology used was proven to be correct.

On the other hand, the elastic constants vs. grain size simulations yielded interesting results. A distinct trend of moduli increasing with grain size can be seen. The results were analyzed further, and it was found that the elastic moduli increase linearly with the percent of atoms in grains. To further this work, it would be of interest to run the same experiments with an even larger grain size to examine if this trend is applicable even up to 50 nm grains, for example.

The results of the nanoindentation also proved to be quite insightful. An inverse Hall-Petch

8. Summary

relationship was shown through decreasing yield stress and hardness with decreasing grain size. The transition point to a typical Hall-Petch relationship was not found within the scale of these experiments, so it can be concluded that it is above 20 nm grain size. Therefore, it would be of interest to analyze larger grain sizes with the same methodology in future work.

Conclusions

- A pairwise potential was shown to sufficiently model polycrystalline CoCrFeMnNi high entropy alloy, by producing values similar to DFT and experiment for a range of mechanical properties.
- The temperature dependence of elastic moduli were calculated using MD methods, and the Young's modulus and shear modulus results align very well with experimental data.
- In polycrystalline systems, the elastic moduli were shown to increase with grain size for grains averaging 4 nm to 20 nm. The relationship of elastic moduli to grain volume fraction was shown to be linear.
- An inverse Hall-Petch relationship was found through nanoindentation tests on grain sizes from 4 nm to 20 nm.

Bibliography

- [1] B. S. Murty, J.-W. Yeh, and S. Ranganathan, “A brief history of alloys and the birth of high-entropy alloys,” (Elsevier, 2014) pp. 1–12.
- [2] J. Piaskowski and C. S. Smith (1963).
- [3] B. Cantor, I. T. H. Chang, P. Knight, and A. J. B. Vincent, *Materials Science and Engineering: A* **375-377**, 213 (2004).
- [4] J.-W. Yeh, S.-K. Chen, S.-J. Lin, J.-Y. Gan, T.-S. Chin, T.-T. Shun, C.-H. Tsau, and S.-Y. Chang, *Advanced Engineering Materials* **6**, 299 (2004).
- [5] J. Liu, X. Guo, Q. Lin, Z. He, X. An, L. Li, L. P. K., X. Liao, L. Yu, J. Lin, L. Xie, J. Ren, and Y. Zhang, *Science China Materials* **62**, 853 (2019).
- [6] B. Gludovatz, A. Hohenwarter, D. Catoor, E. H. Chang, E. P. George, and R. O. Ritchie, *Science* **345**, 1153 (2014).
- [7] B. C. Hu, Y. J. Chang, A. C. Yeh, and Y. J. Chen, *Procedia Manufacturing* **15**, 364 (2018).
- [8] B. Gludovatz, A. Hohenwarter, K. V. S. Thurston, H. Bei, Z. Wu, E. P. George, and R. O. Ritchie, *Nature Communications* **7**, 10602 (2016).
- [9] M. A. Hemphill, T. Yuan, G. Y. Wang, J. W. Yeh, C. W. Tsai, A. Chuang, and P. K. Liaw, *Acta Materialia* **60**, 5723 (2012).
- [10] Z. Tang, T. Yuan, C.-W. Tsai, J.-W. Yeh, C. D. Lundin, and P. K. Liaw, *Acta Materialia* **99**, 247 (2015).
- [11] D. Modupeola, P. Patricia, A. Samson, and M. Ntombi, “High entropy alloys for aerospace applications,” in *Aerodynamics*, edited by G.-B. Mofid and A. Aly-Mousaad (IntechOpen, Rijeka, 2019) Book section 7.
- [12] M. Khruschov, *Wear* **28**, 69 (1974).

- [13] M. A. Moore, *Wear* **28**, 59 (1974).
- [14] F. Haque, *Surface Engineering* **19**, 255 (2003).
- [15] A. C. Fischer-Cripps, “Nanoindentation of thin films,” in *Nanoindentation* (Springer New York, New York, NY, 2004) pp. 132–143.
- [16] L. Qian and H. Zhao, *Micromachines (Basel)* **9** (2018).
- [17] R. Gröger, V. Vitek, and A. Dlouhý, *Modelling and Simulation in Materials Science and Engineering* **28**, 075006 (2020).
- [18] A. P. Thompson, H. M. Aktulga, R. Berger, D. S. Bolintineanu, W. M. Brown, P. S. Crozier, P. J. in ’t Veld, A. Kohlmeyer, S. G. Moore, T. D. Nguyen, R. Shan, M. J. Stevens, J. Tranchida, C. Trott, and S. J. Plimpton, *Computer Physics Communications* **271**, 108171 (2022).
- [19] W. C. Swope, H. C. Andersen, P. H. Berens, and K. R. Wilson, *The Journal of Chemical Physics* **76**, 637 (1982).
- [20] M. S. Daw, S. M. Foiles, and M. I. Baskes, *Materials Science Reports* **9**, 251 (1993).
- [21] Y. Wu, W. H. Liu, X. L. Wang, D. Ma, A. D. Stoica, T. G. Nieh, Z. B. He, and Z. P. Lu, *Applied Physics Letters* **104** (2014).
- [22] G. Laplanche, P. Gadaud, O. Horst, F. Otto, G. Eggeler, and E. P. George, *Journal of Alloys and Compounds* **623**, 348 (2015).
- [23] M. S. Daw and M. I. Baskes, *Physical Review Letters* **50**, 1285 (1983).
- [24] M. I. Baskes, *Phys. Rev. B* **46**, 2727 (1992).
- [25] W.-M. Choi, Y. H. Jo, S. S. Sohn, S. Lee, and B.-J. Lee, *npj Computational Materials* **4**, 1 (2018).
- [26] H. C. Andersen, *The Journal of Chemical Physics* **72**, 2384 (2008).
- [27] S. Nosé, *The Journal of Chemical Physics* **81**, 511 (1984).
- [28] W. G. Hoover, *Phys. Rev. A* **31**, 1695 (1985).
- [29] A. K. Kaw, *Mechanics of Composite Materials* (CRC Press, 2005).
- [30] S. M. C. van Bohemen, *Scripta Materialia* **69**, 315 (2013).
- [31] Y. S. Touloukian, R. Kirby, R. Taylor, and P. Desai, *Thermal expansion: metallic elements and alloys* (IFI/Plenum New York, 1975).

-
- [32] W. Voigt, E. P. Fernandez, and S. L. Hsia, *Journal of Biological Chemistry* **245**, 5594 (1970).
- [33] A. Reuss, *Zeitschrift Angewandte Mathematik und Mechanik* **9**, 49 (1929).
- [34] R. Hill, *Proceedings of the Physical Society. Section A* **65**, 349 (2002).
- [35] S. Tripathi, R. A. Cotter, S. Utamsing, M. M. Islam, M. B. Kivy, and A. Strachan, “Random and special quasirandom structure generator,” (2019).
- [36] P. Hirel, *Computer Physics Communications* **197**, 212 (2015).
- [37] A. Travesset, *The Journal of Chemical Physics* **141** (2014).
- [38] A. Stukowski, *Modelling and Simulation in Materials Science and Engineering* **18** (2010).
- [39] T. Teramoto, K. Yamada, R. Ito, and K. Tanaka, *Journal of Alloys and Compounds* **777**, 1313 (2019).
- [40] E.-W. Huang, D. Yu, J.-W. Yeh, C. Lee, K. An, and S.-Y. Tu, *Scripta Materialia* **101**, 32 (2015).
- [41] H. Ge, H. Song, J. Shen, and F. Tian, *Materials Chemistry and Physics* **210**, 320 (2018).
- [42] G. M. Stoica, A. D. Stoica, M. K. Miller, and D. Ma, *Nature Communications* **5**, 5178 (2014).
- [43] B. I. Koval’chuk and A. A. Lebedev, *Strength of Materials* **4**, 598 (1972).
- [44] B. Gludovatz, E. P. George, and R. O. Ritchie, *Journal of Materials* **67**, 2262 (2015).
- [45] A. J. Zaddach, C. Niu, C. C. Koch, and D. L. Irving, *Journal of Materials* **65**, 1780 (2013).
- [46] R. Gaillac, P. Pullumbi, and F.-X. Coudert, *Journal of Physics: Condensed Matter* **28**, 275201 (2016).
- [47] A. Haglund, M. Koehler, D. Catoor, E. George, and V. Keppens, *Intermetallics* **58**, 62 (2015).
- [48] P. G. Sanders, J. A. Eastman, and J. R. Weertman, *Acta Materialia* **45**, 4019 (1997).
- [49] G. E. Fougere, L. Riester, M. Ferber, J. R. Weertman, and R. W. Siegel, *Materials Science and Engineering: A* **204**, 1 (1995).
- [50] H. S. Kim and M. B. Bush, *Nanostructured Materials* **11**, 361 (1999).

- [51] C. Zhang, B. Han, and M. Shi, “The effects of grain size and temperature on mechanical properties of coCrNi medium-entropy alloy,” (2022).
- [52] O. Deluigi, F. J. Valencia, D. Tramontina, N. Amigo, J. Rojas-Nunez, and E. Bringa, *Crystals* **13**, 357 (2023).
- [53] H. D. Merchant, G. S. Murty, S. N. Bahadur, L. T. Dwivedi, and Y. Mehrotra, *Journal of Materials Science* **8**, 437 (1973).
- [54] D.-H. Lee, M.-Y. Seok, Y. Zhao, I.-C. Choi, J. He, Z. Lu, J.-Y. Suh, U. Ramamurty, M. Kawasaki, T. G. Langdon, and J.-i. Jang, *Acta Materialia* **109**, 314 (2016).
- [55] C. Suryanarayana, D. Mukhopadhyay, S. N. Patankar, and F. H. Froes, *Journal of Materials Research* **7**, 2114 (1992).
- [56] N. Bhate, R. Clifton, and R. Phillips, *AIP Conference Proceedings* **620**, 339 (2002).
- [57] D. N. Blaschke, L. Burakovsky, and D. L. Preston, *Journal of Applied Physics* **130**, 015901 (2021).
- [58] Y. Kamimura, K. Edagawa, and S. Takeuchi, *Acta Materialia* **61**, 294 (2013).
- [59] E. Hall, *Proceedings of the Physical Society. Section B* **64**, 747 (1951).
- [60] N. Petch, *Journal of Iron and Steel Institute* **174**, 25 (1953).
- [61] S. N. Naik and S. M. Walley, *Journal of Materials Science* **55**, 2661 (2020).
- [62] G. D. Hughes, S. D. Smith, C. S. Pande, H. R. Johnson, and R. W. Armstrong, *Scripta Metallurgica* **20**, 93 (1986).
- [63] A. H. Chokshi, A. Rosen, J. Karch, and H. Gleiter, *Scripta Metallurgica* **23**, 1679 (1989).
- [64] B. R. Kuhr and K. E. Aifantis, *Materials Science and Engineering: A* **745**, 107 (2019).
- [65] W. Xu and L. P. Dávila, *Materials Science and Engineering: A* **710**, 413 (2018).
- [66] J. Schiøtz and K. W. Jacobsen, *Science* **301**, 1357 (2003).
- [67] L. Zhang and Y. Shibuta, *Materials Letters* **274**, 128024 (2020).
- [68] W. H. Liu, Y. Wu, J. Y. He, T. G. Nieh, and Z. P. Lu, *Scripta Materialia* **68**, 526 (2013).
- [69] M. R. Jones, B. L. Nation, J. A. Wellington-Johnson, J. F. Curry, A. B. Kustas, P. Lu, M. Chandross, and N. Argibay, *Scientific Reports* **10**, 10151 (2020).

- [70] L. Löfler, *Defects and their influence on mechanical properties in nitrides: an atomistic study*, Phd thesis, Montanuniversität Leoben, Leoben, AT (2022).
- [71] G. Ziegenhain, H. M. Urbassek, and A. Hartmaier, *Journal of Applied Physics* **107** (2010).
- [72] K. L. Johnson and K. L. Johnson, *Contact mechanics* (Cambridge University Press, 1987).
- [73] J.-M. Collin, G. Mauvoisin, and R. El Abdi, *Mechanics of Materials* **40**, 401 (2008).
- [74] Z. Lu, A. Chernatynskiy, M. J. Noordhoek, S. B. Sinnott, and S. R. Phillpot, *Journal of Nuclear Materials* **467**, 742 (2015).
- [75] E. Lilleodden, J. Zimmerman, S. Foiles, and W. Nix, *Journal of the Mechanics and Physics of Solids* **51**, 901 (2003).
- [76] S.-V. Kontomaris, *Micro and Nanosystems* **10** (2018).
- [77] Z. Zeng, M. Xiang, D. Zhang, J. Shi, W. Wang, X. Tang, W. Tang, Y. Wang, X. Ma, Z. Chen, W. Ma, and K. Morita, *Journal of Materials Research and Technology* **15**, 1920 (2021).